Characterization, axial anisotropy and formation conditions of celestine from the Jabal Eghei (Nuqay) late Neogene – Pleistocene volcanic province, southern Libya: Constraints on the mineralogical geothermometer

Pavle Tančić[1,3], Maja Milošević[2], Darko Spahić[3,*], Bojan Kostić[2], Aleksandar Kremenović[2], Maja Poznanović-Spahić[3], Jovan Kovačević[3]

[1]University of Belgrade, Institute of Chemistry, Technology and Metallurgy, Department for Catalysis and Chemical Engineering-National Institute of the Republic of Serbia, Njegoševa 12, 11000 Belgrade, Serbia, Pavle Tančić, E-mail: pavletan@gmail.com (http://orcid.org/0000-0002-4024-710X);

[2]University of Belgrade, Faculty of Mining and Geology, Đušina 7, 11000 Belgrade, Serbia, Maja Milošević, E-mail: maja.milosevic@rgf.bg.ac.rs (https://orcid.org/0000-0002-0520-1413); Bojan Kostić, E-mail: bojan.kostic@rgf.bg.ac.rs (https://orcid.org/0000-0002-8746-8516); Aleksandar Kremenović, E-mail: aleksandar.kremenovic@rgf.bg.ac.rs (https://orcid.org/0000-0001-8845-2332)

[3]Geological Survey of Serbia, Rovinjska 12, 11000 Belgrade, Serbia, [*]**Corresponding author: Dr Darko Spahić**, E-mail: darkogeo2002@hotmail.com (https://orcid.org/0000-0002-5832-0782); Maja Poznanović Spahić, E-mail: maja_poznanovic@yahoo.com (https://orcid.org/0000-0001-9060-0859); Jovan Kovačević, E-mail: jovan.kovacevic@sbb.rs

Abstract: Five celestine crystals are sampled from the (paleo)surface intervening between the late Miocene to Pleistocene basaltic sequences of the Jabal Eghei(Nuqay) volcanic province (southern Libya). The celestine specimens are characterized by applying the combination of the SEM-WDS, ICP/OES, XRPD, and IR methods. The celestine minerals are further analyzed for their color variations and minerogenetic framework. Three samples have greenish-blue-to-blue (480.4-482.5 nm), whereas the other two samples have blue-green color (cyan; 489.1-494.1 nm). The color purity ranges from 1.36-7.16. Their similarity of chemical content is fitting into the celestine near-end members, in which exclusively 1.6-4.1 at. % of Sr^{2+} content was substituted by Pb^{2+} (0.7-0.9 at. %), Ba^{2+} (0.5-0.7 at. %) and Ca^{2+} (0.2-0.8 at. %). The

DOI: 10.1180/mgm.2023.88

composition includes vacancies ranging from 1.0 to 1.9 at. % (observed only in three samples). The content of other chemical elements is minor. The resulting unit-cell parameters have the following ranges: a_0=8.3578(9)-8.3705(6) Å; b_0=5.3510(5)-5.3568(4) Å; c_0=6.8683(7)-6.8767(2) Å and V_0=307.17(5)-308.34(4) Å^3. The XRPD and IR results are mainly in accordance with the SEM-WDS results, having a higher level of correlativity. However, the analysis exposed a few discrepancies yielding several possible interpretations. The illustrated discrepancies were primarily caused by a slight unit-cell axial anisotropy i.e., thermal expansion. In this manner, the results yield a new geothermometric tool that is based on the unit-cell axial anisotropy. The investigated celestines were formed during a Miocene intraplate volcanism, basaltic magmas, and associated brines lifted by the structural conduits (normal faults crosscutting the Sirt basin). The Sr-bearing fluids were then poured into and over the faulted and fractured lagoon-type gypsum, anhydrite Eocene sediments. The celestine minerals were produced within a ~ 368-430K (~ 95-157 °C) temperature range. The celestine is formed at slightly elevated temperature and pressure conditions, close to the shallow subsurface environment (over 250 bars).

Keywords: celestine, characterization, axial anisotropy, formation conditions, Jabal Eghei (Nuqay) volcanic province, southern Libya.

1. Introduction: Overview of the celestine-bearing environments

Celestine ($SrSO_4$; ideally containing 56.42% SrO and 43.58% SO_3) is a common sulfate mineral occurring in the Earth's crust, representing an important raw material frequently used for the production of a critical element strontium (Palache et al. 1951; Deer et al. 2013; see Zhu et al. 2022). Strontium has been used in electronics, ceramics, pigments, cosmetics, papermaking, high-temperature solid lubricants, etc. (e.g., Li et al. 2008). Coupled together with anglesite ($PbSO_4$), celestine belongs to the sulfates of barite ($BaSO_4$) group. These are isostructural minerals crystallizing in the orthorhombic *Pnma* (*Pbnm*) space group (N° 62). They are characterized by the tetrahedral SO_4 anion and cations of considerably

https://doi.org/10.1180/mgm.2023.88 Published online by Cambridge University Press

large size (M=Sr^{2+}, Pb^{2+} and Ba^{2+}), the latter falling into the twelve-coordination with oxygen. The SO_4 tetrahedra and MO_{12} polyhedral share their edges. Notably, anhydrite ($CaSO_4$) differs structurally (space group *Cmcm*, N° 63) from celestine, primarily because of a relatively smaller-in-size Ca^{2+} ion, thus being excluded outside of the barite group (Hanor 2000). Twinning in the celestine could be different and crystals may contain many deffects, at least if they are grown from gels (Patel and Bath, 1972).

Available statistical reports on naturally occurring celestine samples show that the composition of a great majority of celestines is close to that of the end members, having Ba and Ca ordinarily present in amounts that range up to have only a few at. %. Globally, reported celestine occurrences are of a dominant sedimentary origin that is related to the evaporitic processes (e.g., Glazner, 1988; Tekin, 2001; Alvaro et al. 2006; Ariza-Rodríguez et al. 2022). These celestine-bearing evaporitic basins of different age ranges are frequently affected by hydrothermal episodes (e.g., Dai et al. 2014; Fristad et al. 2017; Dhote et al. 2021). Alternatively, celestine minerals occur as fracture and rock cavity fillings (including caves) precipitated by migrating strontium-bearing groundwater or basinal brines ("celestitization"; e.g., Hou et al. 2007). These celestine-bearing brines are poured into carbonate rocks, concretions (e.g., Reolid et al. 2019; Allouche et al. 2023), and nodules (including agate gemstones; Götze et al. 2020). In addition, celestine occurrence can have the format of hydrothermal veins associated with mafic volcanism (e.g., Baskina et al. 1978; Brigatti et al. 1997; Radivojević et al. 2015; Garcia et al. 2016; Tortelli et al. 2022) or basaltic dykes (Anenburg et al. 2014). Occurrences of younger Quaternary celestines comparable to those investigated in southern Libya are barely recorded (e.g., McFadden et al. 1987; Garcia et al. 2016).

Celestines have often been associated with gypsum, anhydrite, native sulfur (evaporites); strontianite, calcite, dolomite, anhydrite, gypsum, fluorite (cavities in carbonate rocks); and also occurring jointly with analcime, natrolite, hydroxyapophyllite, celadonite (mafic volcanoclastics). The presence of the celestine can be the mark of a redox environment (Hadji et al. 2019). On the other hand, anhydrite,

https://doi.org/10.1180/mgm.2023.88 Published online by Cambridge University Press

celestine, and analcime are rarely observed within the borate deposits (Helvaci, 1995). There is a case from Bohemian massif (Czech Republic) describing eclogite as a carrier of Sr-sulfate celestine (Nakamura et al. 2010). Celestine color could range from colorless to blue, to have white, yellow, orange, reddish, greenish, or brownish colors (e.g., brownish celestine from the shear zone in nearby Egypt; El-Sheriff, 2013). The blue color has often been unequally distributed within the mineral growth zones or *face loci*, whereas in some cases blue color could be produced by the irradiation (Palache et al. 1951; Hanor 2000; Deer et al. 2013).

Fig. 1 Here

Several celestine minerals were collected during the Field Geological Mapping campaign of the central and southern Libyan desert [Figs. 1 and 2, including Figure S1 in the electronic supplementary material (hereinafter ESM)]. Field-mapping campaign lasted from 2005 up to 2010, carried out in cooperation between the Industrial Research Centre (Tripoli, Libya) and the Geological Survey of Serbia (former Geoinstitute, Belgrade, Serbia; Figure S1b in the ESM; Toljić and Turki, 2007a,b; Toljić et al. 2007; Rundić and Daloub, 2007; Vasić and Sheriff, 2007; Toljić and Abu Agrab, 2014, 2016). The field mapping campaign encompassed the areas in and around the two magmatic provinces: (i) central Libyan Al Haruj volcanic system (Fig. 1e and Figure S1c in the ESM) that is spatially interconnected with a southern-positioned Neogene to Quaternary segment of the famous Sirt basin, and (ii) the Tibesti–Sirt arch or Jebel Eghei area (Rusk 2001; Cvetković et al. 2010, 2022; Kovačević et al. 2015; Radivojević et al. 2015; Elshaafi and Gudmundsson, 2016, 2017). Spatially, the Al Haruj province of Central Libya contacts the investigated southern-positioned Jabal Eghei Volcanic Province (Cvetković et al. 2010; Radivojević et al. 2015; Elshaafi and Gudmundsson, 2017; Fig. 1c,d; Fig. 2). The occurrence of the celestine minerals in both Libyan volcanic provinces indicates the presence of the two mineral modes: (i) "sedimentary celestine", often embodied in abundant surfacing druses or clusters occurring either in the

https://doi.org/10.1180/mgm.2023.88 Published online by Cambridge University Press

sedimentary formations or within a weathered surface crust (paleosoil) (Fig. 2b,c; Toljić and Turki, 2007; Vasić and Sheriff, 2007; Abdusahmin, 2020), whereas the second type is (ii) magmatic celestine, often surfacing as fracture-related mineral infill (Radivojević et al. 2015).

The following study of the well-preserved celestine minerals collected from the Jabal Eghei Volcanic Province (Fig. 2c,d and Figure S1d,e in the ESM) provides the constraints on the origin of the selected surface-exposed very young celestine crystals (from druses or clusters). The Jabal Eghei celestine minerals are characterized by applying the Scanning Electron Microscopy-Wavelength Dispersive Spectroscopy (hereinafter SEM-WDS), Inductively Coupled Plasma Optical Emission Spectroscopy (hereinafter ICP/OES), X-ray powder diffraction (hereinafter XRPD) and Infrared spectroscopic (hereinafter IR) methods. The study unravels their chemical composition, further characterizing the unit-cell parameters (hereinafter UCPs), and vibrational spectra. In addition to the applied methods, we put constraints on the celestine color variations, including the color purities. Despite very few papers dealing with the origin of the North African (e.g., Anenburg et al. 2014) and in particular central-southern Libyan basalts and associated celestine occurrences (e.g., Elshaafi and Gudmundsson, 2017; Radivojević et al. 2015; Cvetković et al. 2022), the new interpretation of the Jabal Eghei celestine provides a better insight into the axial anisotropy of the investigated celestine crystals and their growth. The regional synthesis deals with the origin of the Jabal Eghei celestine minerals, yielding its formation temperature, and a set of other subsurface conditions under which the investigated crystals were formed. The study further shows that the origin of the Jabal Eghei celestine is similar to that of the Al Haruj basalt area (Fig. 1b).

Fig. 2 Here

2. Regional geological setting: Al Haruj and Jabal Eghei (Nuqay) areas

https://doi.org/10.1180/mgm.2023.88 Published online by Cambridge University Press

There are four principal volcanic provinces in the Central Sahara Desert, whereby a Libyan segment stretches from the Mediterranean coast towards the southern borderland of Libya: 1. Gharayan, 2. As Sawda, 3. Al Haruj Al Aswad, and 4. Jabal Nuqai or Jabal Eghei (Fig. 1b). The youngest are the central Saharan intra-plate mainly basalt volcanic provinces referred to as the Al Haruj and the Jabal Nuqay or Jabal Eghei (central and southern Libya; Fig. 1b and Figure S1c,d in the ESM; Elshaafi and Gudmundsson 2016; Radivojević et al. 2015). The extruded large magmatic provinces and their surrounding host a number of occurrences of near-surface celestine-bearing systems (Rundić and Daloub, 2007; Toljić and Turki, 2007a,b; Toljić et al. 2007; Vasić and Sheriff, 2007; Toljić and Abu Agrab, 2014, 2016; Abdusahmin, 2020). In the field, the investigated celestine mineral clusters are associated either with a sedimentary (*e.g.*, gypsum, anhydrite; Rundić and Daloub, 2007; Toljić and Turki, 2007b; Vasić and Sheriff, 2007; Rundić et al. 2012) or are observed directly on the basaltic rock assemblages (Toljić et al. 2007; Cvetković et al. 2010; Radivojević et al. 2015; Figs. 1c,d,e, 2a,b,c). Both provinces are accommodated along the central-southern realm of the NW-SE striking Sirt basin, whereas the Jabal Eghei province reaches an uncovered segment of the African basement referred to as the Tibesti massif (Toljić and Shagroni, 2007; Le Heron et al. 2013; Radivojević et al. 2015; Abdusahmin, 2020; Fig. 1b and Figure S1c,d,e in the ESM).

2.1. Sirt basin and Al Haruj magmatic-sedimentary province as northern celestine-bearing assemblage

The northern branch of the Cenozoic tectonomagmatic system corresponds to the top-sealing Tertiary segment of the famous oil and gas-bearing Sirt Basin (Rusk 2001; Ashour et al. 2012; Fig. 1b and Figure S1c in the ESM). The underlying Lower Cretaceous Tethyan rift system (Gumati and Nairn, 1991; van der Meer and Cloetingh, 1993; Hallett 2002; Abadi et al. 2008; Capitanio et al. 2009) triggered the Late Cretaceous regional faulting and subsidence contributing the (i) elevation of magma

https://doi.org/10.1180/mgm.2023.88 Published online by Cambridge University Press

into the upper crust and episodic infiltration of hydrothermal fluids (e.g., Toljić and Turki 2007a; Khalifa and Morad 2012; Elshaafi and Gudmundsson, 2016, 2017). Subsidence produced a 4,5 km thick overburden (El-Khatri et al. 2015) allowing deposition of (ii) a number of Paleogene formations that are widespread across the Sirt basin (Toljić and Turki, 2007b; Rundić and Dalub, 2007; Vasić and Sheriff, 2007; Rundić et al. 2012) (onset of the subsidence stage at Cenomanian-Turonian; Rusk 2001). In terms of the oil exploration "language", the syn-rift sedimentary loading of the newly developed accommodation space lasted from the Cretaceous to the Eocene, whereas the post-rift subsidence and deposition continued during the Oligocene and Miocene. The oldest exposed rocks are Eocene Ypresian – Lutetian, Lutetian-Bartonian and late Middle Eocene stages produced in shallow sea, lagoon-type environments, whereas the two overlying sequences are of the Oligocene and Lower to Middle Miocene age (Dur-at-Talah and Maradah formations; Rundić and Dalub, 2007; Toljić and Turki, 2007; Vasić and Sheriff, 2007; Ashour et al. 2012; see Rundić et al. 2012, for details). These Eocene celestine sedimentary carriers (druses) have mainly the form of subhorizontal layers of lagoon-type mixed clastics, limestone, evaporates, and evaporitic limestone sequences, stretching from the Al Haruj Basaltic complex further into the Jebel Eghei area (Abdusahmin, 2020; Fig. 1b; 2a,b,c and Figure S1c,d,e in the ESM). The fibrous gypsum deposits fill out the bedding planes and vertical fractures (post-depositional feature or 'secondary gypsum'; Ashour et al. 2012).

2.2. Jebel Eghei magmatic-sedimentary province as southern celestine-bearing assemblage

The Jabal Eghei basaltic volcanic province is situated in southern Libya (Fig. 1b and Figure S1d,e in the ESM), representing an outcropping fragment of the north-western edge of the Tibesti Mts. The basalts extruded over a superposed metamorphic basement and sedimentary rocks (including the Tertiary Formations similar to those in the Sirt basin; Toljić et al. 2014; Radivojević et al. 2015; Abdusahmin 2020). The older part of this metamorphic-sedimentary assemblage is represented by the continental

https://doi.org/10.1180/mgm.2023.88 Published online by Cambridge University Press

Neoproterozoic to Cambrian Mourizide Formation (Le Heron et al. 2013). A younger part of the sedimentary cover belongs to the Sirt basin, its southernmost periphery. It is composed of the Paleocene–Oligocene sediments, which include the Jabal Eghei basalts (Fig. 2a). In addition to the Cretaceous rifting, the extensional faulting across the Sirt basin likely contributed to the continental crustal opening and extrusion of the basalts across the southern sector or the Jabal Eghei province (Radivojević et al. 2015; Elshaafi and Gudmundsson, 2017; Cvetković et al. 2020; Abdusahmin, 2020).

The recent systematic K/Ar radiometric dating of the Jabal Eghei volcanism pinpoints the Middle Miocene (~16 Ma) to mid-Pleistocene activity (<1 Ma; Radivojević et al. 2015). The three different volcanic phases include: the oldest phase occurred in Middle - to Late Miocene time (basalts show K/Ar age range from 16.1±2.9 to 7.9±2.3 Ma), the second phase having the age range from 7.19±0.36 to 4.32±0.35 Ma, and the youngest extrusion stage occurred at 3.1±1.1 to 0.97±0.68 Ma. The investigated celestine samples are mapped on top of the first volcanic extrusion phase, in the weathered crust (Fig. 2b), accommodated in the intervening position between the second and the third basalt outflow magmatic episodes (Lower Pliocene to Middle Pleistocene; Fig. S1e in the ESM). Considering the mapped extensive celestine presence in the Eocene formations (Toljić and Turki, 2007; Vasić and Turki, 2007; Abusahmin, 2020) and the intense multi-phased basaltic volcanic extrusions (Cvetković et al., 2010; Radivojević et al. 2015; Elshaafi and Gudmundsson, 2017), it is not conceivable to tie the exact time of the Sr-producing hydrothermal activity without the following geothermometrical analysis on celestine minerals.

3. Materials and methods

3.1. Materials

Large crystals (up to 12 cm long; Fig. 2c) were hand-picked during the field-mapping campaign from druses or clusters exposed on the surface. Among the sampled crystals, five well-formed euhedral to

https://doi.org/10.1180/mgm.2023.88 Published online by Cambridge University Press

subhedral samples were chosen. The choice was based on their macroscopically visible different characteristics, *e.g.*, color, luster, transparency, shape, size, and cleavage (Fig. 2d).

3.2. Methods

The analyzed 1-5 samples do not show any radioactivity (measured *in situ* by the Saphymo-SRAT S.P.P.2 NF scintillometer, manufactured by Saphymo-PHY, Massy, France).

The electron microprobe analyses (EMPA) and back-scattered (BSE) images, were obtained on the polished sample surface, by using JEOL JSM-6610LV scanning electron microscope. This microscope is equipped with a wavelength-dispersive spectrometer (Oxford Instruments Wave 700). Operating conditions were at 30 kV accelerating potential, 10 nA beam current, and 2 µm spot size dimension. Standards used for this analytical method were natural and synthetic mineral standards, including celestine (Sr), wollastonite (Ca), barite (Ba and S,) and galenite (Pb).

The contents of the set of trace elements (Ag, As, Al, Be, Bi, Cd, Ce, Co, Cr, Cu, Fe, Ga, Ge, Hf, Hg, Mg, Mn, Mo, Nb, Ni, P, Pb, Sb, Sc, Se, Sm, Sn, Ti, Tl, W, Y, Zn, Zr) and REE (lanthanides, and Th) are characterized by using the ICP/OES technique (Spectro Blue, Germany). Measurements were performed after total decomposition of the samples by fusion with $NaKCO_3$ at 1000 °C, and dissolution with HCl.

XRPD measurements were conducted on a Rigaku Smartlab X-ray Diffractometer, in θ-θ geometry (the sample in a horizontal position). We used the parafocusing Bragg-Brentano geometry using a D/teX Ultra 250 strip detector, in the 1D standard mode having $CuK\alpha_{1,2}$ radiation source (U = 40 kV and I = 30 mA). The XRPD patterns were collected in the 5-90° 2θ range, with the step of 0.01°, and data collection speed of 6.15 °/min. The low background single crystal silicon sample holder is used to minimize the background.

https://doi.org/10.1180/mgm.2023.88 Published online by Cambridge University Press

The unit-cell parameters were calculated and refined using the Le Bail (1988) method. The sequence of the full-matrix least-squares fittings was refined by changing the UCPs (a_0, b_0, and c_0), 100 parameters for the background description, Eta (p-v) parameter, parameters for the description of the halfwidths (U, V, and W) and zero point; until the refinements approached convergence.

The IR spectroscopic analyses were performed by using a Perkin Elmer 597 spectrometer, by applying the KBr pellet method (2 mg of sample and 200 mg of KBr). Visible and near-infrared absorption spectrums were measured in the region 1600–200 cm^{-1}.

The dominant wavenumbers of color for the raw celestine samples were measured with a diffuse reflectance apparatus (400–700 nm), by using a CCS200 spectrometer (Thorlabs). This spectrometer is equipped with an optical fiber wire and is calculated according to the Commission Internationale de l'Eclairage (1932).

The contents of the organic matter were detected by loss of ignition at 600 °C.

4. Results

4.1. SEM-WDS study

The sample-based SEM-WDS analyses yielded homogeneous chemistry results, revealing no zoning in Sr, Ca, Ba, Pb, or S within the samples and various mineral phases (Figure S2 in the ESM and Table 1). The results show similar chemical contents among the analyzed celestine samples. Namely, the major SrO and SO_3 contents have the range of 54.33-55.21 (Δ_{SrO}=0.88) and 43.23-43.93 (Δ_{SO3}=0.70) wt. %, respectively. Among minor oxides, PbO, BaO, and CaO are in the range of 0.87-1.04 (Δ_{PbO}=0.17), 0.42-0.62 (Δ_{BaO}=0.20), and 0.07-0.24 (Δ_{CaO}=0.17) wt. %, respectively. These fit into the major celestine minerals having minor anglesite, barite, and anhydrite substituted components.

Table 1 Here

https://doi.org/10.1180/mgm.2023.88 Published online by Cambridge University Press

According to the calculated apfu's (Table 1), it was observed that samples 1 and 4 show ideal (or almost ideal) stoichiometry, between M and S ions; including the crystal-chemical formulas of $(Sr_{0.984}Pb_{0.009}Ba_{0.005}Ca_{0.002})SO_4$ and $(Sr_{0.978}Pb_{0.008}Ca_{0.008}Ba_{0.007})_{1.001}SO_4$, respectively. On the other hand, samples 2, 3, and 5 show a minor non-stoichiometry, having a small deficit of M cations of *ca.* 1, 1, and 2 at. %, respectively. Accounting that the sulfur content shows a slight excess from the value of 1, we preliminarily suppose that such deficit was induced by a tentative presence of the sum of the total (hereinafter X): H^+ and/or $(H_3O)^+$ and/or OH^- (from H_2O); and/or vacancies. These, for example, could not be depicted accounting for the limitations of the WDS method. Accordingly, the crystal-chemical formulas of samples 2, 3 and 5 could be presented as $(Sr_{0.970}X_{0.010}Pb_{0.008}Ba_{0.007}Ca_{0.005})S_{1.003}O_4$, $(Sr_{0.973}X_{0.010}Pb_{0.007}Ba_{0.005}Ca_{0.005})S_{1.003}O_4$ and $(Sr_{0.959}X_{0.019}Pb_{0.008}Ba_{0.007}Ca_{0.007})S_{1.006}O_4$, respectively. Therefore, we concluded that all studied samples are mutually similar and suit the celestine near-end members, in which only 1.6-4.1 at. % of Sr^{2+} content (Δ_{Sr}=2.5 at. %) is substituted by Pb^{2+} (0.7-0.9 at. %), Ba^{2+} (0.5-0.7 at. %), Ca^{2+} (0.2-0.8 at. %), and the X (1.0-1.9 at. %; in three samples) component. The apfu content of Sr, between the samples, shows an increase of 5<2<3<4<1, whereas the ratios of the Σ(Pb+Ba)/Σ(Ca+X) increase according to 5<3<2<4<1.

By using the apfu's 12-coordinated M^{2+} cations, *i.e.*, Ca^{2+}, Sr^{2+}, Pb^{2+}, and Ba^{2+} derived from the WDS results (Table 1) and their ionic radiuses (r_M) of 1.34Å, 1.44Å, 1.49Å, and 1.61Å, respectively (Shannon, 1976), we have calculated the theoretical ionic radiuses of these cations (Table 2). The results show that the calculated occupancies of the twelve-coordination site are as expected, being also mutually quite similar, further attesting to the previously suggested similarities among the analyzed samples (Δ_{occ}=1.99 at. %). This further includes the deficit of the M cations of ca. 1, 1, and 2 at. % at samples 2, 3, and 5, respectively. In this case, the increase is in a slightly different order of 5<3<2<1<4.

Table 2 Here

https://doi.org/10.1180/mgm.2023.88 Published online by Cambridge University Press

4.2. ICP/OES study

The content of the detected trace elements by using the ICP/OES method is presented in Table 3. We underline that all other analyzed elements (see Chapter 3.2. Methods, for details) are below a detection limit of 0.011-0.500 $mgkg^{-1}$. Consequently, we concluded that all of the analyzed elements should be neglected.

Table 3 Here

4.3. XRPD study

The resulting XRPD patterns [Figure S3 (column I) and Table S1 in the ESM] demonstrate that the observed inter-planar spacings (d_{obs}) are very similar (all samples), and are in line with the celestine ICDD-PDF's 89-0953 (Burger et al. 1998) and 05-0593 (Swanson and Fuyat 1953) reference standards. Because no other minerals are detected, these samples should be interpreted as exclusively the monomineral phases, corroborating the SEM-WDS results. On the contrary, the observed intensities (I_{obs}) show a remarkable difference relative to the applied standards. For example, the strongest standards reflection (*hkl* 211) are with the relative intensity ratios (hereinafter RIR), reaching solely up to only 25 % (sample 1). In addition, a comparative presentation of the reflections with various Miller's *hkl* indices shows a significant variety in the correlations between the analyzed samples (Figure S4 in the ESM). Namely, samples 3 and 5 show distinctively higher RIR's that are directed towards the axis c_0, *i.e.*, the [*00l*] direction (*hkl's*: 002, 004 and 006; Figure S4a, g,j in the ESM). The rest of the reflections, *i.e.* samples 1, 2, and 4 have a higher RIR's value (Table S1 in the ESM). On the other hand, samples 2 and 4 show a less prominent trend inclining towards the axis b_0, *i.e.*, [*0k0*] direction (*hkl's*: 020 and 040; Figures S4e right and S4i left in the ESM), as well as towards the *hkl* 323 (Figure S4h in the ESM). Such differences could be induced by the preferred orientation, accounting for (i) a variety in the cleavage properties (*i.e.* {001} perfect, {210} good and {010} poor; Palache et al. 1951; Deer et al. 2013).

https://doi.org/10.1180/mgm.2023.88 Published online by Cambridge University Press

Differences can be also caused (ii) by epitaxial growth of the celestine on anhydrite (Forjanes et al. 2020b). We also took into consideration the significant presence of calcium in all specimens (Table 1). In addition, differences could also be produced by the structural variation(s), which will be analyzed later.

By using the equation of Goldish (1989), we have calculated the content of the substituted $SrSO_4$ mole fractions (Table 4). Taking into account that this equation is valid for the barite-celestine solid solution (and hence obtained results should be treated cautiously), we tentatively presumed that from 0.2 (samples 1 and 5) to 2.4 (sample 4) mole fractions of $SrSO_4$ were replaced by $BaSO_4$. However, because the Pb^{2+} cation (Table 1) has slightly larger values than Sr^{2+}, yet smaller than Ba^{2+} (Shannon, 1976), these molar substitutions of $SrSO_4$ should exhibit a slightly larger presence. On the other hand, from 0.2 (sample 3) to 0.6 mol. % (sample 2) of $SrSO_4$ could be replaced by a smaller one (such as $CaSO_4$, for example) or caused by the vacancies at the *M* site. Accordingly, the maximal difference of the $SrSO_4$ content among the investigated samples is about 3 mol. %, having the substitutions increasing in the following order: 2<3<1=5<4.

Table 4 Here

The UCPs were calculated and refined by using the Le Bail profile fitting method [Figures S3 (column II) and S5; and Table S2 in the ESM], and presented in Table 5. As expected from the observed inter-planar spacings (d_{obs}, Table S1 in the ESM), all of the calculated UCPs are fairly similar fitting additionally into the reference data standards. However, it could be indicative that different-type variations between the samples are present. Namely, the a_0 and c_0 axes show 2<3<5<1<4, for the volume V_0 it is 2<3<1~5<4, whereas for the b_0 axis has 2<1<3~5<4 variations.

Table 5 Here

https://doi.org/10.1180/mgm.2023.88 Published online by Cambridge University Press

With regards to the mutual correlations between the UCPs (and for all further, as well) variations, the following statistical data are calculated with the MS Excel program, *i.e.* we delivered the coefficients of the regression-R^2 (hereinafter correlations-C). These correlations, reported in our previous studies of different materials (Cvetković and Tančić, 2019; Tančić et al. 2021; Maksimović et al. 2023) are proven useful accessory tools, which allow the comparison between various parameters. According to the results, the polynomial variations between the a_0, c_0, and V_0 parameters are slightly better than the linear (Figure S6 in the ESM), suggesting the deviations from Vegard's law, which is in concordance with the results of Goldish (1989) and Antao (2012). A very high positive correlation C(1) is associated with the a_0 by c_0; a_0 by V_0; and c_0 by V_0 parameters of 0.999; 0.985; and 0.990; respectively. The variations of the b_0 axis by a_0, c_0, and V_0 parameters (Figure S7 in the ESM) display slightly lower, yet likewise very high positive correlation C(2) of 0.880; 0.951; and 0.956; respectively. The positions of the polynomial variations of the investigated samples (Figures S6 and S7 in the ESM) with regards to the celestine, anglesite, and barite reference standards (ICDD-PDF's: 89-0953, 36-1461 and 24-1035, respectively) are also outlined (Figure S8 in the ESM). A lower C(2) correlativity for the variations may be significant, accounting for the relationship with the larger angle declinations documented between the celestine-anglesite and the celestine-barite solid-solutions joins (Figure S8a,c,e in the ESM). Such differently angled declinations were induced by a different expansion behavior of the UCPs, ranging between the Sr^{2+}-Pb^{2+}, Sr^{2+}-Ba^{2+}, and Pb^{2+}-Ba^{2+} substitutions, *i.e.*, between the various solid-solutions series. Namely, the calculated differences in this study (Table S3 in the ESM) show that the highest expansion behavior is among the a_0 and c_0 axes, and the volume V_0. On the other hand, different substitutions do not significantly affect the b_0 axis.

4.4. IR study

https://doi.org/10.1180/mgm.2023.88 Published online by Cambridge University Press

The major vibrational areas exist in the regions between 435-475, 602-650, 995-1005, 1080-1192, and 1200-1248 cm^{-1} (Figure S9 in the ESM and Table 6). Two broad bands were observed across all investigated samples falling in the region between 435 and 475 cm^{-1} and they are more pronounced in samples 1 and 2, respectively to the other samples. The vibrational band that is on 613-614 cm^{-1} is highly pronounced in samples 1 and 2, whereas its position in sample 3 is slightly shifted towards 608 cm^{-1}. The most prominent shift is observed in samples 4 and 5, having the band peak at 602 and 604 cm^{-1}, respectively. A smaller doublet is visible between 610 and 622 cm^{-1}. This doublet is observed on the 622 cm^{-1} for samples 1 and 2, it is shifted to 612 cm^{-1} in sample 3, whereas in samples 4 and 5, it is observed on the 609 and 610 cm^{-1}, respectively. The vibrational features in the region 995-1005 cm^{-1} are also more pronounced in samples 1 and 2, once compared to the rest of the investigated samples. The region between 1080 and 1248 cm^{-1} is a complex group of bands, wherein some of them have the form of a doublet band.

Table 6 Here

Minerals from the barite group are isostructural, resulting in vibrational spectra that are mutually similar, whereas additional spectral features have the form of a small offset. The latter is the result of different associated cations in the structure (Lane 2007). The internal vibrational features present in solid-state sulfates are appearing at *ca.* 1050-1250 (ν3), ~1000 (ν1), ~500-700 (ν4), and ~400-500 (ν2) cm^{-1}. These occur as the result of the asymmetric and symmetric stretching and bending of the SO_4 anion (Herzberg, 1945; Nakamoto, 1986; Vassallo and Finnie, 1992; Bishop and Murad, 2005; Lane, 2007), including the lattice vibrations at ca. 550 cm^{-1} and less (Serna et al. 1986; Clark, 1999; Lane, 2007). The ν1 band is known to be significantly stronger and better pronounced than the ν2 band, which is usually not observable in the infrared spectra of sulfates (Hezel and Ross, 1966; Lane, 2007). Lane (2007) reported that a single ν2 band at 471 cm^{-1} is visible in the spectrum of celestine, whereas Ross (1972,

https://doi.org/10.1180/mgm.2023.88 Published online by Cambridge University Press

1974) observed this band at *ca.* 491 cm^{-1}. As reported by Ross (1974) and Moenke (1962), the ν2 bands are identified at ~465 and ~420 cm^{-1} within the transmission spectrum. According to Lane (2007), the spectral features for Sr as a major element in the celestine are evident at 1238 and 1138 cm^{-1} for ν3. The ν4 band is evident on 648 and 614 cm^{-1}, whereas on 991 cm^{-1}, the ν1 band is observable. Moenke (1956) reports that the deformations of the SO_4 tetrahedra in the optically uniaxial sulfates occur as a doublet on 620 and 1150 cm^{-1} bands. The isomorphous substitution of Sr and Ba typically occurs in the series of barite group of minerals, in particular, between celestine and barite, although celestine may contain a limited amount of Ca^{2+} (Bernstein 1979).

Considering that the Ca^{2+} ion is almost of the same size as Na^{+}, we also take into consideration that substitution between these two ions may also have been occurring. The hypothesis is that K^{+} ions have a higher likelihood to replace Sr^{2+} in the structure than Na^{+}, which in turn has a similar ion radius to the K^{+} ion. As a result, the charge imbalance from this substitution could be compensated with the additional Na^{+} or H^{+} substitutions (Bernstein 1979). The WDS analyses of the investigated samples (Table 1) show that the contents of K_2O and Na_2O are below the detection limit, indicating that these elements are not present in the substitutional positions in the structure. However, PbO, BaO, and CaO are present considerably. The vibrational features of Ba have a slight offset towards the Sr vibration bands that are documented on 1220, 1128 (ν3); 641, 611 (ν4); 981 cm^{-1} (ν1) (Lane 2007). The shift of the high-frequency position of the ν3 fundamental bands is recorded in the sulfate series with Ca^{2+}, in which the ν3 band occurs at a lower-frequency (lower wavenumber) position (Lane 2007). The spectral features of ν3, ν4, and ν1, are systematically offset to smaller wavenumbers for the sulfates containing Pb (ν3 = 1183, 1054; ν4 = 632, 598; ν1 = 960 cm^{-1}) sulfates (Lane 2007). The results are highly correlative with the rest of the applied methods, in particular the SEM-WDS and XRPD, indicating that the samples are of a monomineral composition.

https://doi.org/10.1180/mgm.2023.88 Published online by Cambridge University Press

4.5. Color study

Considering the purity of the color observed in the celestine samples, and the fact that color represents the saturation or its shade, samples 1, 2, and 4 exhibit several nuances ranging between 480 and 482 nm (Table 7). This corresponds with a greenish-blue to blue color, *i.e.* between 492 and 455 nm. Due to the observed color purity, these shades are close to the purest white (Figure S10 in the ESM). On the other hand, samples 3 and 5 exhibit a dominant wavenumber in the range that corresponds to blue-green (cyan) color. Sample 3 has the lightest shade of the color (Table 7) that is nearest to a pure white represented by the illuminator. Sample 5 has the most intense color shade, exposing the purity of the color farthest from the pure white, once compared to the rest of the celestine samples (see Figure S10 in the ESM).

Table 7 Here

5. Discussion

5.1. Disagreements between the WDS and the XRPD results

A few discrepancies are indicative ranging between the WDS and the XRPD results (Tables 1, 2, 4, and 5). Namely, considering different variation trends between the samples, samples 3 and 5 have changed the place with sample 2 (5<3<2<1<4 vs. 2<3<5<1<4; Tables 2 and 5), whereas sample 1 have changed own position just in a few places, belonging the sample 4 {5<2<3<4<1 (apfu contents of Sr) and 5<3<2<4<1 [ratios Σ(Pb+Ba)/Σ(Ca+X)] vs. 2<3<5<1<4; Tables 1 and 5}. Thus, there is a poor correlation C(3) of the ionic radiuses (Table 2) variations by the a_0, b_0, c_0, and V_0 UCPs (Table 5) presented in Figure S11 and Table S4 in the ESM. Optionally, the interpretation of these disagreements could be reached by assessing the presumed structural and/or compositional circumstances, such are: (i) poorly calculated UCPs; and/or (ii) the wrong apfu's basis; and/or (iii) the presence of other previously undetected mineral phases; and/or (iv) the incomplete calculation of ionic radiuses; and/or (v) the option that the palette of

https://doi.org/10.1180/mgm.2023.88 Published online by Cambridge University Press

the structural variations within the samples could take place. Despite seemingly perplexing or even (in)significant, we believe that the listing of these possible reasons could be of the highest importance. The importance lies in avoiding any eventual misleading interpretations.

(i) The study emphasizes the Le Bail (1988) method because the comprehensive experiments were previously applied to the barite group of minerals (Kuang et al. 2017; Li et al. 2018; Girard et al. 2019; Ye et al. 2019). As was previously shown, very good profile parameters and relatively low-reliability factors are characterized by this method (Table S2 in the ESM), a satisfactory level of quality of the resulting difference plots [Figures S3 (column II) and S5 in the ESM], and a very high positive correlations C(1) and C(2) among the UCPs (Figures S6 and S7 in the ESM). Such results corroborate that the investigated samples are suitable for celestines and its *Pnma* structural model. In addition, considerably lower estimated standard deviations (Table 5), which are mostly better even than the reference standards used, provide the validation of the UCPs calculation and refinement. Therefore, we rejected this as a possible reason for the aforementioned disagreements.

(ii) We calculated the apfu's by using the 4 oxygen anions (Table 1), which led to the estimated theoretical ionic radiuses of the M cations (Table 2). Another option allows that the apfu's could be also calculated at the 2 (ΣM+S) ions basis. For example, Antao (2012) provides celestine-derived $(Sr_{0.966}Fe_{0.001}Ba_{0.001})_{0.968}(SO_4)_{1.027}$ chemical formula, which fits the calculated $(Sr_{0.953}Fe_{0.001}Ba_{0.001})_{0.955}S_{1.016}O_4$ (F and Cl apfu's in both cases has the same values, *i.e.* 0.002 and 0.004, respectively; Table S5 in the ESM). As expected, there are no significant differences for samples 1 and 4; whereas samples 2, 3, and 5, show a slightly higher content of Sr, S, and O ions. The results demonstrate that the samples have mutual similarity, fitting into the celestine near-end members, having only 1.6-3.5 at. % of Sr^{2+} content (Δ_{Sr}=1.9 at. %), substituted by the same content of Pb^{2+} (0.7-0.9 at. %), Ba^{2+} (0.5-0.7 at. %) and Ca^{2+} (0.2-0.8 at. %). The variations of the apfu content of the Sr and Σ(Pb+Ba)/Σ(Ca+X) ratios remained identical, *i.e.*,

https://doi.org/10.1180/mgm.2023.88 Published online by Cambridge University Press

5<2<3<4<1 and 5<3<2<4<1, respectively. The only difference is a slightly lower content of the X component (0.7-1.3 at. %; Δ_X=0.3-0.6 at. %) which in turn, leads to a slightly higher calculated ionic radiuses for the aforementioned three samples, and their 5<3<2<4<1 variation (Table S6 in the ESM). However, the resulting correlations [C(4); Figure S12 and Table S4 in the ESM] among these ionic radiuses variations by the a_0, b_0, c_0, and V_0 parameters (Table 5), are significantly less correlative than C(3). Such a low correlativity allows rejection of this possibility as well.

(iii) Although the observed chemical composition is rather simple (Table 1), the X component could hypothetically indicate the presence of other mineral phases, such as gypsum ($CaSO_4 \times 2H_2O$), anhydrite ($CaSO_4$), native sulfur (S), and calcite ($CaCO_3$). It is well known that these mineral phases have often been occurring in the paragenesis with celestine (Palache et al. 1951; Deer et al. 2013). In addition, there is a possibility of the presence of numerous other minerals, such as anglesite, barite, strontianite ($SrCO_3$), aragonite ($CaCO_3$), cerussite ($PbCO_3$), hydrocerussite [$Pb_3(CO_3)_2(OH)_2$], witherite ($BaCO_3$), $SrSO_4 \times 1/2H_2O$ phase (Takahashi et al. 1993) etc., making the interpretation even more complex. To check the eventual presence of anhydrite (samples 1 and 4) and gypsum, including other minerals with the X component (samples 2, 3, and 5), we implemented additional recalculations of the WDS analyses (Table S7 in the ESM). These recalculations are based on the CaO component, the apfu's deficit of the M cations; including the sulfur excess (Table 1), and the theoretical chemical composition of the aforementioned possibly involved minerals.

According to the results, it could be speculated that there is a tentative minor content of: a) anhydrite in samples 1 (0.17 mol. %) and 4 (0.58 mol. %); b) gypsum in the samples 2 (0.49 mol. %), 3 (0.46 mol. %), and 5 (0.68 mol. %); and c) other minerals with the X component in the samples 2 (0.10 mol. %), 3 (0.30 mol. %), and 5 (0.60 mol. %). If this content is taken into account, it appears quite logical and understandable that these minerals couldn't be detected by the XRPD method, because of

https://doi.org/10.1180/mgm.2023.88 Published online by Cambridge University Press

their quantity that is below a detection limit of about 1-2 %. We include a close inspection of the 2θ angle regions, which are fitting into the strongest reflections for these phases (Figure S3 in the ESM). In addition, the WDS method could have failed to separate these from the celestine, mainly because of the similarities in the chemical composition and its limitations in detecting some elements (already mentioned before). The apfu's calculation of 12-coordinated M^{2+} cations (Table S7 in the ESM) was recalculated by applying the theoretical ionic radiuses of these cations (Table S8 in the ESM). The new correlations [C(5); Figure S13 in the ESM] of such ionic radiuses by the a_0, b_0, c_0, and V_0 parameters, despite having a considerably better fit than the C(3) (Table S4 in the ESM) are still quite far from the ideal case. Therefore, this option does not provide a complete explanation of the previously discussed discrepancies and their link with the XRPD results, thus having a tentative character.

In contrast, the presence of other minerals with the X component in the paragenesis with the celestine (although with the desired 2<3<5<1<4 variations) should be rejected, accounting for their lower correlativity [C(6); Figure S14 in the ESM] in comparison with the previously considered two options [*i.e.* C(3) and C(5); Table S4 in the ESM].

(iv) According to the apfu's deficit of the M cations in samples 2, 3, and 5 (Table 1), uncoupling it with other chemical elements which should be neglected (Table 3), we are opinion that the theoretical ionic radiuses need another recalculation. This time by adding the appropriate sulfur excess of 0.3, 0.3, including 0.6 at. % of the S^{6+} taken from the tetrahedral site (0.12 Å in coordination IV; Shannon, 1976), respectively. The two options are chosen (Table S9 in the ESM): (1) monomineral celestines (Table 2), and (2) major celestines that barely have any anhydrite or gypsum (Table S8 in the ESM). A similar correlation of these ionic radiuses by the a_0, b_0, c_0, and V_0 parameters is observed in these two cases [C(7) and C(8); Figures S15 and S16, and Table S4 in the ESM]. However, neither the first nor the second option do not reach any improvement, in regards to these from the C(3). Consequently, this

https://doi.org/10.1180/mgm.2023.88 Published online by Cambridge University Press

correlation should also be rejected as a possible explanation for the aforementioned variances. At last, the single remaining solution should be taken into consideration.

(v) Although the crystal structure refinements are beyond the scope of this paper, our previous studies of diverse mineral species, and solid solutions, have demonstrated that the different UCPs, polyhedral distortions, site occupancy factors, bond lengths, bond angles, valence units, etc., could be influenced either by (a) different inserted cations into the mineral structure; and/or by (b) diverse conditions of their formation, in particular, the temperature and pressure (Tančić 2017, 2018; Tančić and Kremenović 2022; Tančić et al. 2012, 2020, 2023).

(a) Whilst considering the affected variations of the UCPs, accounting for the different inserted cations into the mineral structure, we initiated the process by introducing the calculations of their presumed values by the multiplication of the Sr, Ca, Pb, and Ba apfu's with the corresponding UCPs of celestine, anhydrite, anglesite and barite reference standards (ICDD-PDF's: 89-0953, 37-1496, 36-1461 and 24-1035, respectively). For the selected apfu's, we have chosen the two previously discussed options: (1) the celestines as the monomineral phases (Table 1); and (2) the option of celestines without the Ca, which hypothetically belongs to minor amounts of gypsum and anhydrite phases (Table S7 in the ESM). The results (presented in Table S10 in the ESM) indicate that the largest differences (Δ) between these presumed values and those of the XRPD method (Table 5) are, valid for both options, occurring in samples 2, 3, and 5. Such correlativity is expected and suited to the already emphasized vacancies and the here-used calculations. Accordingly, the ratios increased by *ca.* 1, 1, and 2 %, respectively. In both cases, we observe excellent correlations of the calculated ionic radiuses (Table 2 and Table S8 in the ESM) by the a_0, b_0, c_0, and V_0 parameters [C(9) and C(10); Figures S17 and S18, and Table S4 in the ESM]. Because both options are almost identical, this couldn't be used as a reliable parameter for the already distinguished factors. On the other hand, these results further indicate that the presumed UCPs should be

https://doi.org/10.1180/mgm.2023.88 Published online by Cambridge University Press

theoretically near the realistic chemical composition. However, as discussed earlier, such a scenario is obviously not the case. Namely, the presumed unit-cell volumes of samples 2, 3, and 5 include an absence of any fitting in no case, because they have significantly lower values, inclusive of the comparison with the anhydrite (ICDD-PDF: 37-1496; V=305.60 $Å^3$) reference standard. Consequently, we observe a very poor correlation between the presumed (Table S10 in the ESM) and determined (Table 5) a_0, b_0, c_0, and V_0 UCPs [C(11); Figure S19 and Table S4 in the ESM].

Thus, we further reconsider the impact of the existing vacancies in the celestine structure on their UCPs. Namely, the available reference data (Table S11 in the ESM) show that there is an example having a significant content of the vacancy of 3 at. % [Antao 2012; already discussed within part (ii)]. This celestine example has more or less similar [ICDD-PDF's: 05-0593 and 89-0953; Table 5; Miyake et al. (1978)], or even larger UCPs, comparative to those without any vacancy [Hawthorne and Ferguson (1975); Jacobsen et al. (1998); Ye et al. (2019)]. Likewise, three selected samples showed identical average <M-O> distances of 2.827(1)Å (Hawthorne and Ferguson 1975; Jacobsen et al. 1998; Antao 2012). Accordingly, it appears that the existing vacancies in the celestine structure do not have any significant impact on their UCPs. The causes for such behavior could be the geometrical changes of the SO_4 and MO_{12} polyhedral, *i.e.*, a decrease of the average <M-O> distance, the charge on the O ions that have more subordinate values, including the average <S-O> distance that is lengthier in this case; or *vice versa* (Antao 2012). In addition, the tetrahedral distortions are a function of the geometry of the structure rather than the chemistry of the twelve-coordinated site (Hawthorne and Ferguson, 1975; Brigatti et al. 1997).

To check the afore-described option, another two variances discussed earlier (ii-iv) yet without the existing vacancies (included for samples 2, 3, and 5) are taken into consideration: (1) celestines as monomineral phases, with previously characterized apfu's (Table 1), including the theoretical ionic radiuses of the M cations with occupancies of the twelve-coordination site (Table 2) that are further

https://doi.org/10.1180/mgm.2023.88 Published online by Cambridge University Press

recalculated (Tables S12 and S13 in the ESM), and (2) as the major celestines with the neglected gypsum or anhydrite phases (including the previously determined apfu's; Table S7 in the ESM). The recalculation includes the theoretical ionic radiuses of the M cations and occupancies of the twelve-coordination site (Table S8 in the ESM), which are given in Tables S14 and S15 in the ESM. The correlations of the recalculated ionic radiuses (Tables S13 and S15 in the ESM) by the a_0, b_0, c_0, and V_0 parameters show: (1) best fit [C(12); Figure S20 and Table S4 in the ESM] of the all available correlations associated with the problematic of the ionic radiuses by UCPs variations [i.e., C(3)-C(8)], including (2) the lowest correlativity among all of these correlations [C(13); Figure S21 and Table S4 in the ESM].

Finally, the newly calculated UCPs are characterized based on the apfu's (Table S12 in the ESM) and are given in Table S16 in the ESM. The correlations between these a_0, b_0, c_0, and V_0 values, with those of the XRPD method (Table 5) have, in this case, an acceptable correlation [C(14); Figure S22 and Table S4 in the ESM], which is significantly better than the previous one associated with this problematic [*i.e.* C(11)]. These observations substantiate the concluding remarks indicating that the existing vacancies in the structures of samples 2, 3, and 5 do not have any significant impact on their UCPs. Such a good correlativity further leads to the conclusion that the complete set of 1-5 samples should be interpreted exclusively as monomineral celestine near-end members, agreeing with the SEM-WDS, XRPD, and IR results. Therefore, the correlativity allows us to finally abandon "option iii" as a probable cause for the earlier discussed disagreements.

(b) The results in Tables S10 and S16 in the ESM demonstrate that there is a slightly different ratio between various crystallographic axes, such as $c_0<a_0<b_0$ (samples 1 and 4), $a_0<c_0<b_0$ (samples 2 and 3) and $a_0=c_0<b_0$ (sample 5). Such diverse ratios indicate the presence of axial anisotropy, which was previously observed and studied for the synthetic and natural end members of the barite group of minerals (see Kuang et al. 2017; Li et al. 2018; Girard et al. 2019; Ye et al. 2019; and references therein, for the

https://doi.org/10.1180/mgm.2023.88 Published online by Cambridge University Press

examples). This phenomenon appears in conditions experiencing an increase in the temperature environment (axial expansion anisotropy) and elevated formation pressure (axial compression anisotropy) conditions. To the best of our knowledge, there is a lack of similar experiments so far, dealing with the solid solutions between minerals within the barite group. Accordingly, we further recalculated the variations of the temperature dependence by the UCPs for the $Clt_{98}Ang_{02}$, $Clt_{96}Ang_{04}$, and $Clt_{94}Ang_{06}$ celestine-anglesite (Table S17 in the ESM) and for the $Clt_{99}Brt_{01}$, $Clt_{98}Brt_{02}$ and $Clt_{97}Brt_{03}$ celestine-barite (Table S18 in the ESM) solid-solution series [mineral name symbols such as Ang, Brt and Clt refer to anglesite, barite, and celestine, respectively (Warr, 2021)]. These recalculations use the combination of the initial experimental data at the ambient pressure for anglesite (Li et al. 2018), celestine, and barite (Ye et al. 2019); according to the suitable cell modification from the *Pbnm* (II) to the *Pnma* (I) space group, constrained as follows: $a_{0I}=b_{0II}$, $b_{0I}=c_{0II}$, and $c_{0I}=a_{0II}$. Such resulting data (i.e., Tables S17 and S18 in the ESM) are further used for the construction of Figure 3. In addition, we also calculated the expansion degree of the UCPs (*i.e.*, their ratio) of celestine, anglesite, and barite between 320K and 520K (Table S19 in the ESM). By using its composition and UCPs, we strongly believe that this method can successfully be applied as a geothermometer.

Fig. 3 Here

By using the recalculated theoretical ionic radiuses of the M cations (Table S13 in the ESM), the excesses of the Sr^{2+}, Ca^{2+}, and Ba^{2+} apfu's, reaching over 1.44 Å, are converted as the total Pb^{2+}, *i.e.* as the anglesite 1.40-3.10 mol. % content in celestine. Similarly, the excesses of Sr^{2+}, $Ca^{2+,}$ and Pb^{2+} apfu's over 1.44 Å are also converted as the total Ba^{2+}, *i.e.* as the barite 0.41-0.91 mol.% content in celestine (Table 8). Subsequently, the Ang and Brt values (Table 8, plotted in Fig. 3) further allowed the estimation of the formation temperatures for the investigated 1-5 celestine samples by using their determined UCPs (Table 5). The results show that a set of very similar temperatures characterizes both the celestine-anglesite and

https://doi.org/10.1180/mgm.2023.88 Published online by Cambridge University Press

the celestine-barite solid-solution series. In that manner, we have the validation of the recalculated Ang and Brt values. The results demonstrate that sample 2 underwent the lowest temperatures reaching as low as ~368K, whereas sample 4 was under the exposure to the highest temperature range reaching ~430K. Samples 1, 3, and 5 were formed at remarkably similar average temperatures of ~387K, ~384K and ~387K, respectively. Therefore, the sampled celestines were formed at the ~368-430K (~95-157 °C) temperature range, at the ambient pressure conditions. Different correlations between the crystallographic axes are $b_0<a_0<c_0$ (samples 1 and 4) and $a_0<b_0<c_0$ (samples 2, 3 and 5).

Table 8 Here

Finally, we exemplify the discussed discrepancies between the WDS and the XRPD results. Namely, Figure S23 in the ESM contains five possible variations (plotted from Fig. 3h; should be taken into account only as an example, because of its validity for each of the other a_0, b_0, and c_0 unit-cell axes, including the Ang contents): 1. volume increase by a temperature increase, including the Brt contents increase; 2. volume increase by a constant temperature, including the Brt contents increase; 3. volume increase by a temperature decrease, including the Brt contents increase; 4. constant volume by a temperature increase, including the Brt contents decrease; and 5. volume increase by a temperature increase, having a constant Brt content. We underline that each of these possible interpretations could be also *vice versa*. In our favorable case, we concluded that the investigated celestine 1-5 samples, are mostly with the first variation type, having partially the fifth variation type, *i.e.*, that their UCPs increased mainly accounting for a temperature increase, whereas the Ang and the Brt contents are reaching almost the constant values (*i.e.*, having a small content difference of Δ_{Ang}=1.70 mol. %, and Δ_{Brt}=0.50 mol. %; Table 8), but also following the increased status. Because samples 3 and 5 were exposed to higher temperatures than sample 2, whereas sample 4 was formed at a higher temperature than sample 1, the former records the larger thermal expansions of the UCPs than the latter. This is the main reason for the average

https://doi.org/10.1180/mgm.2023.88 Published online by Cambridge University Press

2<3<1~5<4 and 2<3~1=5<4 UCPs variation behaviors (Tables 5 and 8, respectively). In addition, samples 3 and 5 have a larger expansion of the b_0 axis, reaching values exceeding those of sample 1; another possible interpretation is that sample 1 was formed at a higher pressure by comparing to samples 3 and 5 because this axis has the largest compressibility (Kuang et al. 2017; Ye et al. 2019). Accordingly, we strongly believe that this argument provides sufficient evidence, to support the interpretation that the formation temperature is the primary cause for the UCPs variations of celestine, whereas different inserted cations into the structure should be interpreted as a secondary factor. To simplify, there is almost a perfect correlativity C(15) of the average temperature dependence (Table 8) by the a_0, b_0, c_0, and V_0 UCPs (Table 5) of 0.965; 0.951; 0.991 and 0.997, respectively (Figure S24 and Table S4 in the ESM). The correlation is superior compared to the C(12) and C(14) correlations of the celestine composition.

By using the extrapolated data (Tables S17 and S18 in the ESM; Table 8 and Fig. 3) we moreover estimate the UCPs of the studied samples formed at a near-room temperature (23 °C), and under the ambient pressure conditions (Table S20 in the ESM). The resulting data are used exclusively for the characterization of the relative UCPs (Table 9). In this case, a wide range of correlations between the crystallographic axes is observed: $b_0<c_0<a_0$ (samples 1 and 4), $a_0<b_0<c_0$ (sample 2), $a_0<c_0<b_0$ (sample 3), and $c_0<b_0<a_0$ (sample 5).

Table 9 Here

The results have almost the perfect correlation C(16) of the average temperature dependence (Table 8), by the a_0, b_0, c_0, and V_0 ratios (Table 9) of 0.979; 0.926; 0.988 and 0.998, respectively (Figure S25 in the ESM). These are, as expected, very similar to the C(15) correlations, observed relative to the temperature by the UCPs variations (Figure S24 in the ESM). In addition, the linear and the polynomial deviations have almost the same values in these two cases.

https://doi.org/10.1180/mgm.2023.88 Published online by Cambridge University Press

The synthesis of data (Tables 8 and 9; Figure S25 in the ESM), allowed us to additionally construct the variation diagram of the relative a_0, b_0, c_0, and V_0 UCPs (*i.e.*, their ratios) by the temperature dependence of the studied samples at the ambient pressure conditions (Fig. 4). Importantly, the resulting variation chart is fitting (*i.e.* for all of the five samples together) with the celestine $c_0<b_0<a_0$ crystal growth expansive behavior (see Figs. 11b and 12b at Ye et al. 2019; and Table S19 in the ESM). Taking into account solely the crystal expansion induced by the elevated temperature (Table 8), samples 1 and 4 show variations that are similar to that of barite, whereas samples 2, 3, and 5 show deviations analogous to that of celestine (Ye et al. 2019; and Table S19 in the ESM). By interpreting the structural aspect (Antao 2012), the first group of samples is less distorted, in comparison with the second, confirming the geometry change of the SO_4 and MO_{12} polyhedral, influenced primarily by the vacancies occupied by the latter ones (already discussed before). On the other hand, taking into account solely the crystal compression by pressure, it appears that sample 4 was also developed at a considerably higher pressure (similarly to sample 1) relative to samples 2, 3, and 5 because of their identical axis variations (Table 9).

Fig. 4 Here

5.2. Celestine minerogenesis and formation conditions

Celestine as a low-temperature mineral has often been associated with magmatic-hydrothermal activity reaching temperatures under 300°C (Anenburg et al. 2014). To reconstruct minerogenesis, we take into consideration celestine formation conditions, in particular, the typifying shallow crustal marine, evaporitic paleoredox environments (Hanor 2000, 2004). Such shallow depths of magma and hydrothermal fluid migration were facilitated by a cluster of faults as part of their conduits in the uppermost basinal segment of the crust (Ashour et al. 2012; Elshaafi and Gudmundssen, 2016). The

https://doi.org/10.1180/mgm.2023.88 Published online by Cambridge University Press

multistage volcanism contributed to the extrusion of primitive and evolving light fractions of basaltic magma (Elshaafi and Gudmundssen, 2017).

The results indicate that the Jebel Eghei celestines were formed at ~368-430K (~95-157 °C) temperature range, at the ambient pressure conditions (Table 8). Consequently, we tested the following options for the Jebel Eghei celestine minerogenesis (Fig. 5): 1. temperature remains constant by a pressure increase; 2. temperature increase by a pressure increase; and 3. temperature increase by a pressure decrease. Following the experimental data (Kuang et al. 2017; Li et al. 2018; Girard et al. 2019; Ye et al. 2019; Curzi et al. 2022), we tested whether, with the increase of subsurface pressure, the temperatures are following the rising trend. Taking into consideration the age of magmatic events, the proposed increasing temperature trend is somewhat aligned with the stage of minor subsidence during the Early Oligocene and Early Miocene (subsidence stage proposed by van der Meer and Cloetingh, 1993). The coupled temperature-pressure elevations have produced the axial compression (by pressure), which should be simultaneously compensated by the axial expansion (by temperature) so that the UCPs remain as already previously characterized (Table 5). Accordingly, we have chosen the second option (see yellow lines in Figure 5), because the other two available options are leading exclusively toward the smaller UCPs. The increasing slope is approximated accounting for the absence of the appropriate experimental data for the formation pressure. Nevertheless, the increase of the formation pressure allowed us to put subsurface constraints on probable subsurface conditions under which the investigated crystals could have been formed. For example, suppose we adjust the subsurface pressure to fit with the resulting temperatures. In that case, we get the pressure of ca. 250 bars or shallow crustal depths up to only a few kilometers under the Earth's surface (Fig. 5). Accordingly, the temperature range is shifted becoming slightly higher, *ca.* 372-434K (~99-161 °C) fitting into the active hydrothermal fluids that were associated with the volcanic areas. To underline, the celestine-producing hydrothermal event occurred likely during the Miocene

https://doi.org/10.1180/mgm.2023.88 Published online by Cambridge University Press

producing the brine which was poured initially into the faulted and fractured Eocene lagoon deposits (Ashour et al. 2012). The subsequent process of precipitation and formation of celestine-bearing druses or nodules (e.g., Anenburg et al. 2014) was likely initiated once the sediments were exposed to the terrestrial conditions. Thus, the celestine druses mapped across the investigated area appear to be the product of the reaction of hypersaline Sr-bearing fluids with gypsum and anhydrite (Hanor 2000, 2004; Forjanes et al. 2020a,b). Both gypsum and anhydrite are mapped across the investigated areas (Al Gata, Tamed Al Kusur, and Krarat Al Jifah Formations; Vasić and Sheriff, 2007; Abdusahmin, 2020).

Fig. 5 Here

On the other hand, subsidence and deposition of sedimentary systems, like these within the Sirt basin (Gumati and Nairn, 1991; van der Meer and Cloetingh, 1993), yield higher pressures than that observed within the surfacing volcanic areas. By presuming a subsidence-related pressure increase, reaching up to 500, 750, 1000, and 1250 bars, the temperature range may increase reaching ~382-444K (~109-171 °C), ~391-453K (~118-180 °C), ~429-482K (~147-209 °C), and ~452-514K (~179-241 °C), respectively (Fig. 5a). In that manner, we provide a reconstruction of the broader temperature range in which the celestine occurred. We further narrowed the celestine formation conditions and its formation depths. As a result, the Jebel Eghei (and likely Al Haruj) celestine minerogenesis occurred at the following subsurface conditions:

1. from ~382K (~109 °C; sample 2), over ~417K (~144 °C; sample 1), ranging to ~482K (~209 °C; sample 4), at 500, 750 and 1000 bars, respectively (Figure 5b); or

2. from ~372K (~99 °C; sample 2), over ~412K (~139 °C; sample 1), ranging to ~453K (~180 °C; sample 4), at 250, 500 and 750 bars, respectively (Figure 5c).

https://doi.org/10.1180/mgm.2023.88 Published online by Cambridge University Press

It is to be noted that expected subsidence trends without overpressure zones can induce pressures of 340 bar or ca. 4931 psi, approximating shallow ca. 1500 m or 4921 foot of burial depth:

$$\rho_{ob} = \rho_l + \rho_f$$

ρ_{ob} is total overburden pressure; ρ_l is lithostatic pressure; ρ_f is fluid pressure; as per Tiab and Donaldson (2012). However, the *P-T* emplacement paths of hydrothermal fluids can have more complex overpressure conditions (Curzi et al., 2022).

6. Conclusion

Five late Neogene to Middle Pleistocene aged celestine crystals are analyzed and characterized for minerogenesis by applying the SEM-WDS, ICP/OES, XRPD, and IR methods. Their chemical composition is very similar and fits into the monomineral celestine near-end members in which only 1.6-4.1 at. % of Sr^{2+} contents were substituted by Pb^{2+}, Ba^{2+}, Ca^{2+} and the vacancies (in three samples). The results emphasize that the subsurface temperatures were related to the hydrothermal fluids associated with voluminous intermittent volcanic activities that are the primary cause of the transport of strontium into the Sirt basin. The investigated celestines were likely formed as a secondary mineral, repositioned into the gypsum and/or anhydrite layer, at temperatures over ~373K (~100 °C) and pressures over 250 bars. The subsequent formation of geodes or druses and nodules is further attributed to the clustering of celestine across sedimentary formations, but under surface conditions (similar to Anenburg et al. 2014). The constraints on the differently inserted Pb^{2+}, Ba^{2+}, and Ca^{2+} cations into the structure are characterized as a secondary factor for the unit-cell parameters expansion, including the observed slight $c_0<b_0<a_0$ axial anisotropy variations. We believe that these slight anisotropy variations could serve as effective new geothermometric tools capable of providing conditions on multiple mineral growth stages. This is of particular importance in exploring the enigmatic relationships between Sr mineralization and igneous rocks (for the complex relationships see Zhu et al. 2022, for a discussion).

https://doi.org/10.1180/mgm.2023.88 Published online by Cambridge University Press

Three celestine samples have a greenish-blue to blue color, whereas the other two samples are of blue-green (cyan) color. In addition, the celestine minerogenesis study of the Jabal Eghei area corroborated that the coefficients of the regression-R^2 may represent a very useful accessory tool pertinent for the mineral's comparison purposes, or once correlating a variety of available parameters.

Except for the larger vacancy content in sample 5, the most prominent difference in the color purity ranges between samples 3 and 5. These samples have very similar results, yielded by several methods used throughout this study. At last, further experiments are necessary to resolve this problem.

Acknowledgements

We are grateful to the Geological Survey of Serbia for allowing us insight into the abundant geological mapping materials and help during writing this paper. This work was financially supported by the Ministry of Education, Science and Technological Development of the Republic of Serbia (Grant No. 451-03-47/2023-01/200026). We also owe our highest gratitude to the editor-in-chief Stuart Mills, an unknown reviewer, as well as Dr Ahmad Rabiee, for significant improvement of the early version of the manuscript.

Declaration of competing interest: The authors have no competing interests to declare.

https://doi.org/10.1180/mgm.2023.88 Published online by Cambridge University Press

References

Abadi, A. M., Van Wees, J. D., Van Dijk, P. M., and Cloetingh, S. A. (2008) Tectonics and subsidence evolution of the Sirt Basin, Libya. *AAPG bulletin*, 92(8), 993-1027. https://doi.org/10.1306/03310806070

Abdusahmin FA (2020) *Geology and potentiality of basalts in Jabal Eghei area (Libya)*. PhD dissertation, Faculty of Mining and Geology, Belgrade, Serbia.

Abouessa, A., Pelletier, J., Duringer, P., Schuster, M., Schaeffer, P., Métais, E., ... and Rubino, J. L. (2012) New insight into the sedimentology and stratigraphy of the Dur At Talah tidal-fluvial transition sequence (Eocene–Oligocene, Sirt Basin, Libya). *Journal of African Earth Sciences*, 65, 72-90. https://doi.org/10.1016/j.jafrearsci.2012.02.004

Allouche, F., Ammous, A., Tlili, A. et al. (2023) Uranium-bearing celestine and barite in the Upper-Paleocene deposits of the Siouf-Cherahil sector: stratigraphic distribution, geochemical, and mineralogical characterization. *Carbonates and Evaporites,* 38, 31. https://doi.org/10.1007/s13146-023-00857-x

Álvaro, J. J., Ezzouhairi, H., Vennin, E., Ribeiro, M. L., Clausen, S., Charif, A., ... and Moreira, M. E. (2006) The Early-Cambrian Boho volcano of the El Graara massif, Morocco: Petrology, geodynamic setting and coeval sedimentation. *Journal of African Earth Sciences*, 44(3), 396-410. https://doi.org/10.1016/j.jafrearsci.2005.12.008

Anenburg, M., Bialik, O. M., Vapnik, Y., Chapman, H. J., Antler, G., Katzir, Y. and Bickle, M. J. (2014). The origin of celestine–quartz–calcite geodes associated with a basaltic dyke, Makhtesh Ramon, Israel. Geological Magazine, 151(5), 798-815. https://doi.org/10.1017/S0016756813000800

Antao, S. M. (2012) Structural trends for celestite (SrSO4), anglesite (PbSO4), and barite (BaSO4): Confirmation of expected variations within the SO4 groups. *American Mineralogist*, 97(4), 661-665. http://dx.doi.org/10.2138/am.2012.3905

Ariza-Rodríguez, N., Rodríguez-Navarro, A. B., Calero de Hoces, M., Martin, J. M., and Muñoz-Batista, M. J. (2022) Chemical and Mineralogical Characterization of Montevive Celestine Mineral. *Minerals*, 12(10), 1261. https://doi.org/10.3390/min12101261

Baskina, V. A., Volchanskaya, I. K., Frikh-Khar, D. I., and Yarmolyuk, V. V. (1978) Potassic alkaline-basic and alkaline volcanic rocks of Southern Mongolia. *International Geology Review*, 20(12), 1426–1440. https://doi.org/10.1080/00206817809471519

Bérar, J. F., and Lelann, P. (1991) ESD's and estimated probable error obtained in Rietveld refinements with local correlations. *Journal of applied crystallography*, 24(1), 1-5. https://doi.org/10.1107/S0021889890008391

Bernstein, L. R. (1979) Coloring mechanisms in celestite. *American Mineralogist*, 64(1-2), 160-168.

Bershov, L. V. and Marfunin, A. S. (1967) Electron-spin resonance of electron-hole centres in minerals. *Doklady Akademii Nauk SSSR*, 173(2), 410-412.

Bishop, J. L. and Murad, E. (2005) The visible and infrared spectral properties of jarosite and alunite. *American Mineralogist*, 90(7), 1100-1107. https://doi.org/10.2138/am.2005.1700

Brigatti, M. F., Galli, E., and Medici, L. (1997) Ba-rich celestine: new data and crystal structure refinement. *Mineralogical Magazine*, 61(406), 447-451. https://doi.org/10.1180/minmag.1997.061.406.10

Capitanio, F. A., Faccenna, C., and Funiciello, R. (2009) The opening of Sirte basin: Result of slab avalanching? *Earth and Planetary Science Letters*, 285(1-2), 210-216. https://doi.org/10.1016/j.epsl.2009.06.019

Commission Internationale de l'Eclairage (1932) 1931 Commission Internationale de l'Eclairage Proceedings. Huitième session. pp. 19–29. Cambridge, UK, Cambridge University Press.

Clark, R. N. (1999) Chapter 1: Spectroscopy of Rocks and Minerals, and Principles of Spectroscopy. In A.N. Rencz, Ed., *Manual of Remote Sensing, Remote Sensing for the Earth Sciences*, 3, 3-58. John Wiley and Sons, New York.

https://doi.org/10.1180/mgm.2023.88 Published online by Cambridge University Press

Curzi, M., Caracausi, A., Rossetti, F., Rabiee, A., Billi, A., Carminati, E., et al. (2022). From fossil to active hydrothermal outflow in the back-arc of the central Apennines (Zannone Island, Italy). Geochemistry, Geophysics, Geosystems, 23, e2022GC010474. https://doi.org/10.1029/2022GC010474

Cvetković, V., Radivojević, M., Prelević, D., Toljić, M. and Turki, S. M. (2022). An insight into the evolution of the lithospheric mantle of south Saharan metacraton: Mantle xenoliths from Jabal Eghei Volcanic Complex, Libya. *Journal of Volcanology and Geothermal Research*, 432, 107691. https://doi.org/10.1016/j.jvolgeores.2022.107691

Cvetković, V., Toljić, M., Ammar, N. A., Rundić, L., and Trish, K. B. (2010) Petrogenesis of the eastern part of the Al Haruj basalts (Libya). *Journal of African Earth Sciences*, 58(1), 37-50. https://doi.org/10.1016/j.jafrearsci.2010.01.006

Cvetković, Ž. and Tančić, P. (2019) Mineralogical and crystallographic characteristics of bauxites from some Grebnik's (Metohija, Serbia) ore deposits. *Geološki anali Balkanskoga poluostrva*, 80(1), 45-61. https://doi.org/10.2298/GABP19010045C

Dai, S., Li, T., Seredin, V. V., Ward, C. R., Hower, J. C., Zhou, Y., ... and Zhao, C. (2014) Origin of minerals and elements in the Late Permian coals, tonsteins, and host rocks of the Xinde Mine, Xuanwei, eastern Yunnan, China. *International Journal of Coal Geology*, 121, 53-78. https://doi.org/10.1016/j.coal.2013.11.001

Deer, W., Howie, R., and Zussman, J. (2013). Celestine. In: *An Introduction to the Rock-Forming Minerals*, 3rd edn The Mineral Society: London, UK, pp. 444

Dhote, P., Bhan, U. and Verma, D. (2021) Genetic model of carbonatite hosted rare earth elements mineralization from Ambadongar Carbonatite Complex, Deccan Volcanic Province, India. Ore Geology Reviews, 135, 104215. https://doi.org/10.1016/j.oregeorev.2021.104215

Doelter, C. (1915) Die Farben der Mineralien. Fried. Vieweg und Sohn, Braunschweig, Germany.

Elshaafi, A., and Gudmundsson, A. (2016) Volcano-tectonics of the Al Haruj Volcanic Province, Central Libya. *Journal of Volcanology and Geothermal Research*, 325, 189–202 10.1016/j.jvolgeores.2016.06.025

Elshaafi, A. and Gudmundsson, A. (2017). Distribution and size of lava shields on the Al Haruj al Aswad and the Al Haruj al Abyad Volcanic Systems, Central Libya. *Journal of Volcanology and Geothermal Research*, 338, 46-62. https://doi.org/10.1016/j.jvolgeores.2017.03.012

El-Khatri, F., El-Ghali, M. A. K., Mansurbeg, H., Morad, S., Ogle, N. and Kalin, R. M. (2015). Diagenetic alterations and reservoir quality evolution OF lower cretaceous fluvial sandstones: Nubian formation, Sirt basin, north-central Libya. Journal of Petroleum Geology, 38(2), 217-239. https://doi.org/10.1111/jpg.12607

El-Sherif, A. M. (2013) Mineralogical characterization of the alteration facies at Gabal El-Missikat Area, Central Eastern Desert, Egypt. *Nuclear Sciences Scientific Journal*, 2(1), 1-21. DOI: 10.21608/nssj.2013.30976

Forjanes, P., Astilleros, J. M., and Fernández-Díaz, L. (2020a) The formation of barite and celestite through the replacement of gypsum. *Minerals*, 10(2), 189. https://doi.org/10.3390/min10020189

Forjanes, P., Gómez-Barreiro, J., Morales, J., Manuel Astilleros, J., Fernández-Díaz, L. (2020b) Epitactic growth of celestite on anhydrite: substrate induced twinning and morphological evolution of aggregates. *CrystEngComm*, 22, 5743–5759. https://doi.org/10.1039/D0CE00755B

Friend, J.N., and Allchin, J.P. (1939) Colour of celestine. *Nature*, 144, 633 https://doi.org/10.1038/144633a0

Friend, J.N., and Allchin, J.P. (1940) Colloidal gold as a colouring principle in minerals. *Mineralogical Magazine*, 25, 584-596 https://doi.org/10.1180/minmag.1940.025.170.03

Fristad, K. E., Svensen, H. H., Polozov, A., and Planke, S. (2017) Formation and evolution of the end-Permian Oktyabrsk volcanic crater in the Tunguska Basin, Eastern Siberia. *Palaeogeography, Palaeoclimatology, Palaeoecology*, 468, 76-87. https://doi.org/10.1016/j.palaeo.2016.11.025

https://doi.org/10.1180/mgm.2023.88 Published online by Cambridge University Press

Gadsden, J.A. (1975) *Infrared Spectra of Minerals and Related Inorganic Compounds*. Butterworth and Co. (Publishers) Ltd., London

Garske, D., and Peacor, D.R. (1965) Refinement of the structure of celestite $SrSO_4$. Zeitschrift fur Kristallographie, 121, 204–210. https://doi.org/10.1524/zkri.1965.121.16.204

Girard, A., Stekiel, M., Spahr, D., Morgenroth, W., Wehinger, B., Milman, V., ... and Winkler, B. (2018) Structural, elastic and vibrational properties of celestite, SrSO4, from synchrotron x-ray diffraction, thermal diffuse scattering and Raman scattering. *Journal of Physics: Condensed Matter*, 31(5), 055703. https://doi.org/10.1088/1361-648X/aaf0ef

Glazner, A. F. (1988) Stratigraphy, structure, and potassic alteration of Miocene volcanic rocks in the Sleeping Beauty area, central Mojave Desert, California. *Geological Society of America Bulletin*, 100(3), 424–435. https://doi.org/10.1130/0016-7606(1988)100<0424:SSAPAO>2.3.CO;2

Goldish, E. (1989) X-ray diffraction analysis of barium-strontium sulfate (barite-celestite) solid solutions. *Powder Diffraction*, 4(4), 214-216. https://doi.org/10.1017/S0885715600013750

Götze, J., Möckel, R., and Pan, Y. (2020) Mineralogy, geochemistry and genesis of agate—A review. *Minerals*, 10(11), 1037. https://doi.org/10.3390/min10111037

Guirguis, L.A. (1987) Infrared vibrational sulphate band shift correlation in alkaline sulphate minerals. *TIZ-Fachberichte,* 111, 339-340

Gumati, M.S., Basin Architecture and Tectonic Controls on the Early Cretaceous Sarir Sandstone Reservoir, Eastern Sirt Basin, Libya, Journal of African Earth Sciences, https://doi.org/10.1016/j.jafrearsci.2020.104089.

Gumati, Y. D. and Nairn, A. E. M. (1991). Tectonic subsidence of the Sirte basin, Libya. Journal of Petroleum Geology, 14(1), 93-102. https://doi.org/10.1111/j.1747-5457.1991.tb00301.x

Hadji, F., Marok, A., and Samet, A. M. (2019) Geochemistry and Mineralogy of the Miocene and Pliocene sediments of the Northern Margin of the Lower Chelif Basin (Western Tellian Domain, North Algeria). In *Petrogenesis and Exploration of the Earth's Interior*. Proceedings of the 1st Springer Conference of the Arabian Journal of Geosciences (CAJG-1), Tunisia 2018 (pp. 109-112). Springer International Publishing.

Hallett, D. (2002) *Petroleum Geology of Libya*. Elsevier, Amsterdam, 503p.

Hanor, J.S. (2000) Barite-Celestine Geochemistry and Environments of Formation. In: Alpers CN, Jambor JL, Nordstrom DK (eds) *Sulfate Minerals-Crystallography, Geochemistry, and Environmental Significance Reviews in Mineralogy and Geochemistry* 40. Virginia: Mineralogical Society of America, Chantilly, pp 193–275

Hanor, J. S. (2004) A model for the origin of large carbonate-and evaporite-hosted celestine (SrSO4) deposits. *Journal of Sedimentary Research*, 74(2), 168-175. https://doi.org/10.1306/092203740168

Hawthorne, F. C., and Ferguson, R. B. (1975) Anhydrous sulphates; I, Refinement of the crystal structure of celestite with an appendix on the structure of thenardite. *The Canadian Mineralogis*t, 13(2), 181-187.

Helvaci, C. (1995) Stratigraphy, mineralogy, and genesis of the Bigadic borate deposits, western Turkey. *Economic Geology*, 90(5), 1237–1260. https://doi.org/10.2113/gsecongeo.90.5.1237

Hezel, A., Ross, S.D. (1966) Forbidden transitions in the infra-red spectra of tetrahedral anions - III. Spectra-structure correlations in perchlorates, sulfates, and phosphates of the formula MXO_4. *Spectrochim Acta*, 22, 1949-1961. https://doi.org/10.1016/0371-1951(66)80183-2

Herzberg, G. (1945) *Infrared and Raman Spectra of Polyatomic Molecules*. Van Nostrand, New York

Hou, Z., Zaw, K., Pan, G., Mo, X., Xu, Q., Hu Y., and Li, X. (2007). Sanjiang Tethyan metallogenesis in SW China: Tectonic setting, metallogenic epochs and deposit types. *Ore Geology Reviews*, 31(1-4), 48-87. https://doi.org/10.1016/j.oregeorev.2004.12.007

ICDD-PDF 05-0593 (1953) Celestine, Swanson, Fuyat, National Bureau of Standards (U.S.), Circ. 539, II, 61

https://doi.org/10.1180/mgm.2023.88 Published online by Cambridge University Press

ICDD-PDF 24-1035 (1972) Barite, National Bureau of Standards (U. S.) Monograph, 25, 10, 12

ICDD-PDF 36-1461 (1986) Anglesite, McMurdie et al. Powder Diffr 1, 70

ICDD-PDF 37-1496 (1986) Anhydrite, McMurdie et al. Powder Diffr 1, 267

ICDD-PDF 89-0953 (1998) Strontium Sulfate, Burger K, Cox D, Papoular R, Prandl W, J Appl Cryst 31:789

Isetti, G. (1970) *Studio sulla colorazione della celestina*. Doriana, 4, no. 194, 1-7

Jacobsen, S. D., Smyth, J. R., Swope, R. J. and Downs, R. T. (1998) Rigid-body character of the SO4 groups in celestine, anglesite and barite. *Canadian mineralogist*, 36, 1053-1060.

Khalifa, M. and Morad, S. (2012). Impact of structural setting on diagenesis of fluvial and tidal sandstones: the Bahi Formation, Upper Cretaceous, NW Sirt Basin, North Central Libya. *Marine and Petroleum Geology*, 38(1), 211-231. https://doi.org/10.1016/j.marpetgeo.2011.05.006

Kloprogge, J.T., Ruan, H., Duong, L.V., Frost, R.L. (2001) FT-IR and Raman microscopic study at 293 K and 77 K of celestine, $SrSO_4$, from the middle Triassic limestone (Muschelkalk) in Winterswijk, The Netherlands. *Geologie en Mijnbouw/Netherlands Journal of Geosciences* 80(2): 41-47 https://doi.org/10.1017/S0016774600022307

Kovačević, J., Tereesh, M. B., Radenković, M. and Miljanić, Š. S. (2013). Discovery of uranium mineralizations in the rhyolite-granite complex in the Jabal Eghei area of southern Libya. *Journal of the Serbian Chemical Society*, 78(5), 741-758. https://doi.org/10.2298/JSC120919124K

Kuang, Y., Xu, J., Zhao, D., Fan, D., Li, X., Zhou, W. and Xie, H. (2017) The high-pressure elastic properties of celestine and the high-pressure behavior of barite-type sulphates. *High Temperatures-High Pressures*, 46, 481-495.

Lane, M. D. (2007) Mid-infrared emission spectroscopy of sulfate and sulfate-bearing minerals. *American Mineralogist*, 92(1), 1-18. https://doi.org/10.2138/am.2007.2170

Le Bail, A., Duroy, H., and Fourquet, J. L. (1988) Ab-initio structure determination of LiSbWO6 by X-ray powder diffraction. *Materials Research Bulletin*, 23(3), 447-452. https://doi.org/10.1016/0025-5408(88)90019-0

Le Heron, D. P., Meinhold, G., and Bergig, K. A. (2013) Neoproterozoic–Devonian stratigraphic evolution of the eastern Murzuq Basin, Libya: a tale of tilting in the central Sahara. *Basin Research*, 25(1), 52-73. https://doi.org/10.1111/j.1365-2117.2012.00555.x

Li, B., Xu, J., Chen, W., Ye, Z., Huang, S., Fan, D., ... and Xie, H. (2018) Compressibility and expansivity of anglesite (PbSO 4) using in situ synchrotron X-ray diffraction at high-pressure and high-temperature conditions. *Physics and Chemistry of Minerals*, 45, 883-893. https://doi.org/10.1007/s00269-018-0970-1

Li, Y. F., Ouyang, J. H., and Zhou, Y. (2008) Novel fabrication of monodispersed peanut-type celestine particles using Sr-EDTA chelating precursors. *Materials Chemistry and Physics*, 111(2-3), 508-512. https://doi.org/10.1016/j.matchemphys.2008.05.008

Maksimović, T., Tančić, P., Maksimović, J., Mara, D., Ilić, M., Van Deun, R., Joksović, Lj. and Pagnacco, M. (2023) Novel cerium and praseodymium doped phosphate tungsten bronzes: Synthesis, characterization, the behavior in the Briggs-Rauscher reaction and photoluminescence properties. *Optical Materials*, 143, 114125. DOI: https://doi.org/10.1016/j.optmat.2023.114125

McFadden, L. D., Wells, S. G., and Jercinovich, M. J. (1987) Influences of eolian and pedogenic processes on the origin and evolution of desert pavements. *Geology*, 15(6), 504-508. https://doi.org/10.1130/0091-7613(1987)15<504:IOEAPP>2.0.CO;2

Miyake, M., Minato, I., Morikawa, H. and Iwai, S. (1978). Crystal structures and sulphate force constants of barite, celestite, and anglesite. *American Mineralogist*, 63(5-6), 506-510.

Moenke,, H. (1959) *Mineralspektren I: Die Ultrarotabsorption der häufigsten und wirtschaftlich wichtigsten Halogenid-, Oxyd-, Hydroxyd-, Carbonat-, Nitrat-, Borat-, Sulfat-, Chromat-, Wolframat-, Molybdat-, Phosphat-, Arsenat-, Vanadat- und Silikatmineralien im Spektralbereich 400-4000 cm*$^{-1}$. Akademie Verlag, Berlin.

https://doi.org/10.1180/mgm.2023.88 Published online by Cambridge University Press

Nakamoto, K. (1986) *Infrared and Raman Spectra of Inorganic and Coordination Compounds*. Wiley and Sons, New York

Nakamura, D., Kobayashi, T., Shimobayashi, N., Svojtka, M., and Hirajima, T. (2010) Sr-sulphate and associated minerals found from kyanite-bearing eclogite in the Moldanubian Zone of the Bohemian Massif, Czech Republic. *Journal of mineralogical and petrological sciences*, 105(5), 251-261. https://doi.org/10.2465/jmps.090817

Omori, K. (1968) Infrared diffraction and the far infrared spectra of anhydrous sulfates. *Mineralogical Journal*, 5(5), 334-354. https://doi.org/10.2465/minerj1953.5.334

Palache, C., Berman, H., Frondel, C. (1951) *Dana's system of mineralogy*, 7th ed., v. II, John Wiley & sons, London, UK, pp. 415–420.

Patel, A.R. and Bhat, H.L. (1972) Growth of single crystals of $BaSO_4$ and $SrSO_4$ from gels. *Journal of Crystal Growth*, 12, 288-290. https://doi.org/10.1016/0022-0248(72)90299-0

Radivojević, M., Toljić, M., Turki, S. M., Bojić, Z., Šarić, K., and Cvetković, V. (2015) Neogene to Quaternary basalts of the Jabal Eghei (Nuqay) area (south Libya): Two distinct volcanic events or continuous volcanism with gradual shift in magma composition?. *Journal of Volcanology and Geothermal Research*, 293, 57-74. http://dx.doi.org/10.1016/j.jvolgeores.2015.02.003

Reolid, M., Abad, I., and Benito, M. I. (2019) Upper Pliensbachian-Lower Toarcian methane cold seeps interpreted from geochemical and mineralogical characteristics of celestine concretions (South Iberian palaeo-margin). *Palaeogeography, Palaeoclimatology, Palaeoecology*, 530, 15-31. https://doi.org/10.1016/j.palaeo.2019.05.033

Ross, S.D. (1972) *Inorganic Infrared and Raman Spectra.* McGraw-Hill Book Company (UK) Ltd., London

Ross, S.D. (1974) Sulphates and other oxy-anions of group VI. In: The Infrared Spectra of Minerals, V.C. Farmer (ed), *Mineralogical Society Monograph* 4, 423-444. https://doi.org/10.1180/mono-4.18

Rundić, Lj., Dalub, H. (2007) *Geological map of Libya 1:250 000. Sheet Dur Al Abrag (NG 34–5)*. Explanatory Booklet. Industrial Research Center, Tripoli. 110 pp.

Rundić, Lj., Toljić, M., Vasić, N., et al. (2012) Tertiary Formations of the SW Part of Sirt Basin: New Stratigraphic and Sedimentological Data. *Geology of Southern Libya*, 1, 153-174

Rusk, D.C. (2001). Libya: Petroleum potential of the underexplored basin centers—A twenty-first-century challenge, in MW Downey, JC Threet, and WA Morgan (eds), *Petroleum provinces of the twenty-first century*, AAPG Memoir 74, p. 429–452.

Schulman, J.H., Compton, W.D. (1962) *Color Centers in Solids*. Macmillan, New York

Serna, C. J., Cortina, C. P., and Ramos, J. V. G. (1986) Infrared and Raman study of alunite—Jarosite compounds. Spectrochimica Acta Part A. *Molecular Spectroscopy*, 42(6), 729-734. DOI: 10.1016/0584-8539(86)80092-7

Shannon, R.D. (1976) Revised Effective Ionic Radii and Systematic Studies of Interatomic Distances in Halides and Chalcogenides, *Acta Crystallographica*, A32, 751-767. https://doi.org/10.1107/S0567739476001551

Stromeyer, F. (1821). *Untersuchungen über Mischung der Mineralkörper*, vol. 1. Vandenhoeck und Ruprecht, Gottingen

Takahashi, S., Seki, M., and Setoyama, K. (1993) Formation of $SrSO_4 \cdot 1/2H_2O$ in an $SrSO_4$–H_2O System and Its Solid Solution in a $CaSO_4$–$SrSO_4$–H_2O System, *Bulletin of the Chemical Society of Japan*, 66(8), 2219-2224. https://www.journal.csj.jp/doi/10.1246/bcsj.66.2219

Tančić, P. (2017) Comparison of the crystallographic-chemical characteristics of sphalerites from the Kiževak ore deposit with some other deposits, part I: Preliminary reconsideration about their formation conditions. *Bulletin of Mines CXIV (1-2)*, 101–117. Doi: 10.25075/BM.2017.11

https://doi.org/10.1180/mgm.2023.88 Published online by Cambridge University Press

Tančić, P. (2018) Comparison of the crystallographic-chemical characteristics of sphalerites from the Kiževak ore deposit with some other deposits, part II: Construction of the four-component a_0-FeS-P-T diagram (option I) and determination of the formation conditions. *Bulletin of Mines CXV (1-2)*, 59–73. Doi: 10.25075/BM.2018.04

Tančić, P., and Kremenović, A. (2022) Rietveld crystal structure refinement of the natural rhombohedral grossular-andradite garnet from Serbia. *Geological Quarterly*, 66(7), 1639. https://gq.pgi.gov.pl/article/view/33000

Tančić, P., Dušanić, S. and Erić, S. (2023): Orthorhombic crystal structure of grossular garnet (Suva Česma, Western Serbia): Evidence from the Rietveld refinement. *Powders*, 2(2), 387–402. DOI: https://doi.org/10.3390/powders2020023

Tančić, P., Kremenović, A. and Vulić, P. (2020). Structural dissymmetrization of optically anisotropic $Grs_{64\pm1}Adr_{36\pm1}Sps_2$ grandite from Meka Presedla (Kopaonik Mt., Serbia). *Powder Diffraction*, 35(1), 7-16. https://doi.org/10.1017/S0885715619000897

Tančić, P., Dimitrijević, R., Poznanović, M., Pačevski, A., and Sudar, S. (2012) Crystal structure and chemical composition of ludwigite from Vranovac ore deposit (Boranja Mountain, Serbia). *Acta Geologica Sinica-English Edition*, 86(6), 1524-1538. https://doi.org/10.1111/1755-6724.12020

Tančić, P. I., Spahić, D. N., Jovanović, D., Ćirić, A., Poznanović-Spahić, M., and Vasić, N. (2021) Occurrences and characterization of alunite group minerals from the Lece-Radan Oligo-Miocene volcanic complex (Serbia). *Geological Quarterly*, 65. https://gq.pgi.gov.pl/article/view/29032

Tekin, E. (2001) Stratigraphy, geochemistry and depositional environment of the celestine-bearing gypsiferous formations of the Tertiary Ulaş-Sivas Basin, East-Central Anatolia (Turkey). *Turkish Journal of Earth Sciences*, 10(1), 35-49. https://journals.tubitak.gov.tr/earth/vol10/iss1/3

Tiab, D., Donaldson, E.C., (2012) Chapter 2 - Introduction to Petroleum Geology, Editor(s): Djebbar Tiab, Erle C. Donaldson, Petrophysics (Third Edition), Gulf Professional Publishing, 27-83, ISBN 9780123838483, https://doi.org/10.1016/B978-0-12-383848-3.00002-5

Toljić, M., and Agrab, A.F.M. (2014) *Geological map of Libya 1:250 000. Sheet Wādi Eghei (NF 34-1)*. Explanatory Booklet. Industrial Research Center, p. 305. Tripoli (in print)

Toljić, M., and Agrab, A.F.M. (2016) *Explanatory Booklet, Sheet: Wadi Eghei (NF 34-1)*. Geological map of Libya 1:250,000, Industrial Research Centre, Libya, Tripoli. p. 30. (in print)

Toljić, M., and Turki, S.E.M. (2007a) *Geological Map of Libya: Mourizidie Sheet (1:250 000) Explanatory Booklet.* Industrial Research Centre, Tripoli, Libya.

Toljić, M., and Turki, S.E.M. (2007b) *Explanatory booklet for the Geological map of Libya, 1:250 000 Sheet NF 34-1*. 326 pp., Beograd –Tripoli.

Toljić, M., Marović, M., Kovačević, J., et al (2007) *Explanatory booklet for the Geological map of Libya, 1:250 000 Sheet NF 34-1*. 326 pp., Beograd –Tripoli.

Tortelli, G., Gioncada, A., Pagli, C., Braschi, E., Gebru, E. F., and Keir, D. (2022) Constraints on the magma source and rift evolution from geochemistry of the Stratoid flood basalts (Afar, Ethiopia). *Geochemistry, Geophysics, Geosystems*, 23(8), e2022GC010434. https://doi.org/10.1029/2022GC010434

van Der Meer, F. and Cloetingh, S. (1993). Intraplate stresses and the subsidence history of the Sirte Basin (Libya). Tectonophysics, 226(1-4), 37-58. https://doi.org/10.1016/0040-1951(93)90109-W

Vasić, N., Sheriff, K.A. (2007) *Geological map of Libya 1: 250,000. Sheet: Dur-At-Talah (NG 34-9)* Explanatory Booklet. Industrial Research Centre, Libya. Tripoli. 180pp.

Vassallo, A. M., and Finnie, K. S. (1992) Infrared emission spectroscopy of some sulfate minerals. *Applied Spectroscopy*, 46(10), 1477-1482. https://doi.org/10.1366/0003702927896192 96

https://doi.org/10.1180/mgm.2023.88 Published online by Cambridge University Press

Warr, L. N. (2021) IMA–CNMNC approved mineral symbols. *Mineralogical Magazine*, 85(3), 291-320. https://doi.org/10.1180/mgm.2021.43

Wittstein, G.C. (1856) *Ueber die Ursache der blauen Farbe des Coelestins*. Vierteljahresschrift für Praktische Pharmacie, 5, 286-287

Ye, Z., Li, B., Chen, W., Tang, R., Huang, S., Xu, J., ... and Xie, H. (2019) Phase transition and thermoelastic behavior of barite-group minerals at high-pressure and high-temperature conditions. *Physics and Chemistry of Minerals*, 46, 607-621. https://doi.org/10.1007/s00269-019-01026-0

Zhu, Q., Cook, N. J., Xie, G., Ciobanu, C. L., Gilbert, S. E., Wade, B., and Xu, J. (2022) Textural and geochemical analysis of celestine and sulfides constrain Sr-(Pb-Zn) mineralization in the Shizilishan deposit, eastern China. *Ore Geology Reviews*, 144, 104814. https://doi.org/10.1016/j.oregeorev.2022.104814

https://doi.org/10.1180/mgm.2023.88 Published online by Cambridge University Press

Figure captions

https://doi.org/10.1180/mgm.2023.88 Published online by Cambridge University Press

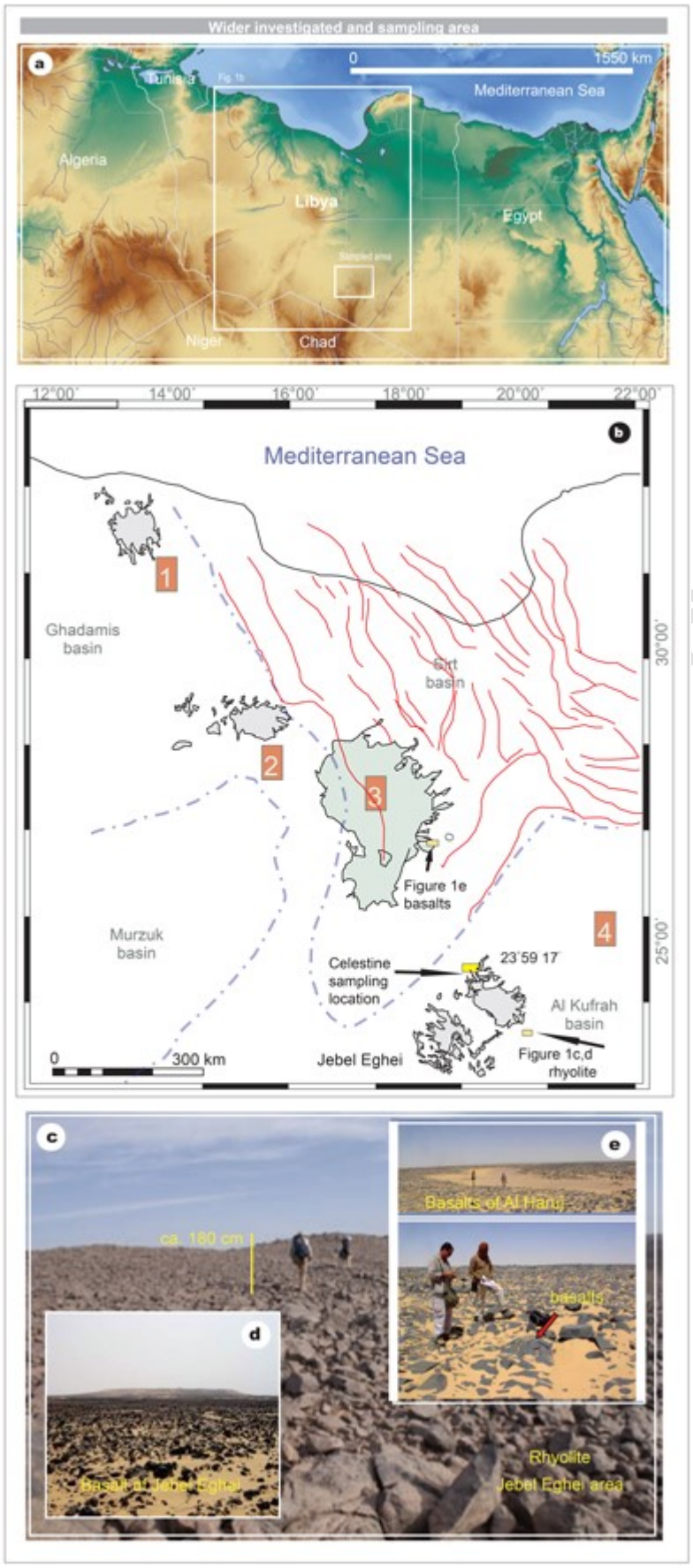

https://doi.org/10.1180/mgm.2023.88 Published online by Cambridge University Press

Figure 1. a Geographical relief map of the wider investigated central-southern Libya; **b** The sketch map showing the distribution of the four main volcanic provinces in Libya and principal faults delineating the celestine-bearing Sirt Basin and Jabal Nuqau Volcanic Province (modified after Elshaafi and Gudmundsson, 2016). The Al Haruj Volcanic Province (#3) is situated on the south-western margin of the Sirt Basin, central Libya. To the south is the Jabal Eghei or Jabal Nuqau Volcanic Province (#4). Other provinces are (#1) Gharayan Volcanic Province, and (#2) As Sawda Volcanic Province; **c** Panoramic view on Jebel Eghei rhyolite volcanic complex (photo taken from Kovačević et al. 2013; modified); **d** at lower left corner are basalts from Jebel Eghei area (Abdusahmin, 2020, modified); **e** at upper right corner are basalts from Al Haruj area (photos taken from Vasić and Sheriff, 2007; modified).

https://doi.org/10.1180/mgm.2023.88 Published online by Cambridge University Press

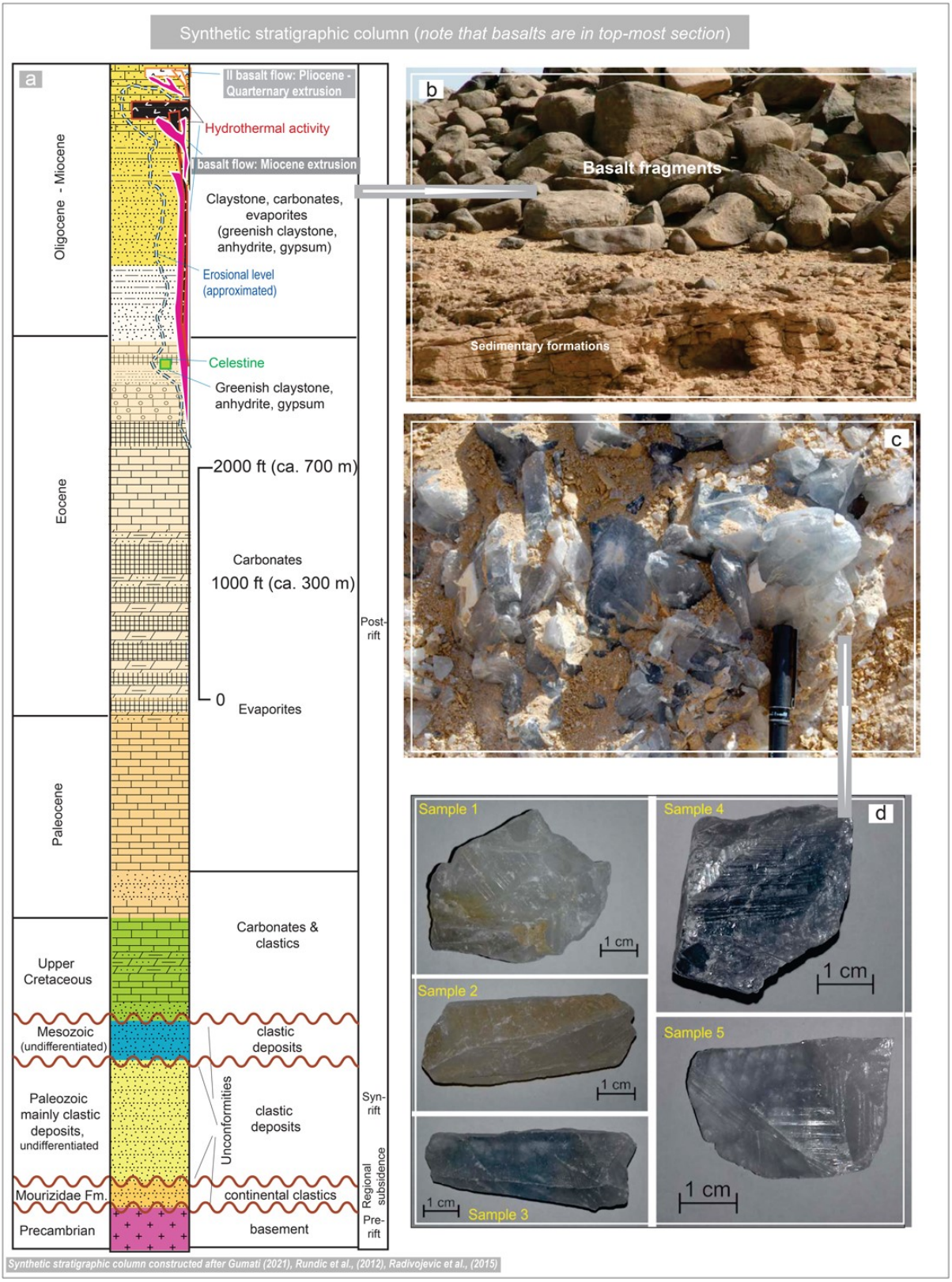

Figure 2. **a** Synthetic stratigraphic column constructed after Gumati (2021), Rundić et al. (2012), and Radivojević et al. (2015); **b** Basalt fragments and sedimentary formations (from Abdusahmin, 2020, modified); **c** Occurrences of

https://doi.org/10.1180/mgm.2023.88 Published online by Cambridge University Press

celestine crystals at the Al Gata member, formation Wadi Thámat (Coordinates: Lat. 23º 53' 17''; Long. 19º 02' 31''). Photo by J. Kovačević; **d** Selected 1-5 celestine samples used in the study. Photos by P. Tančić;

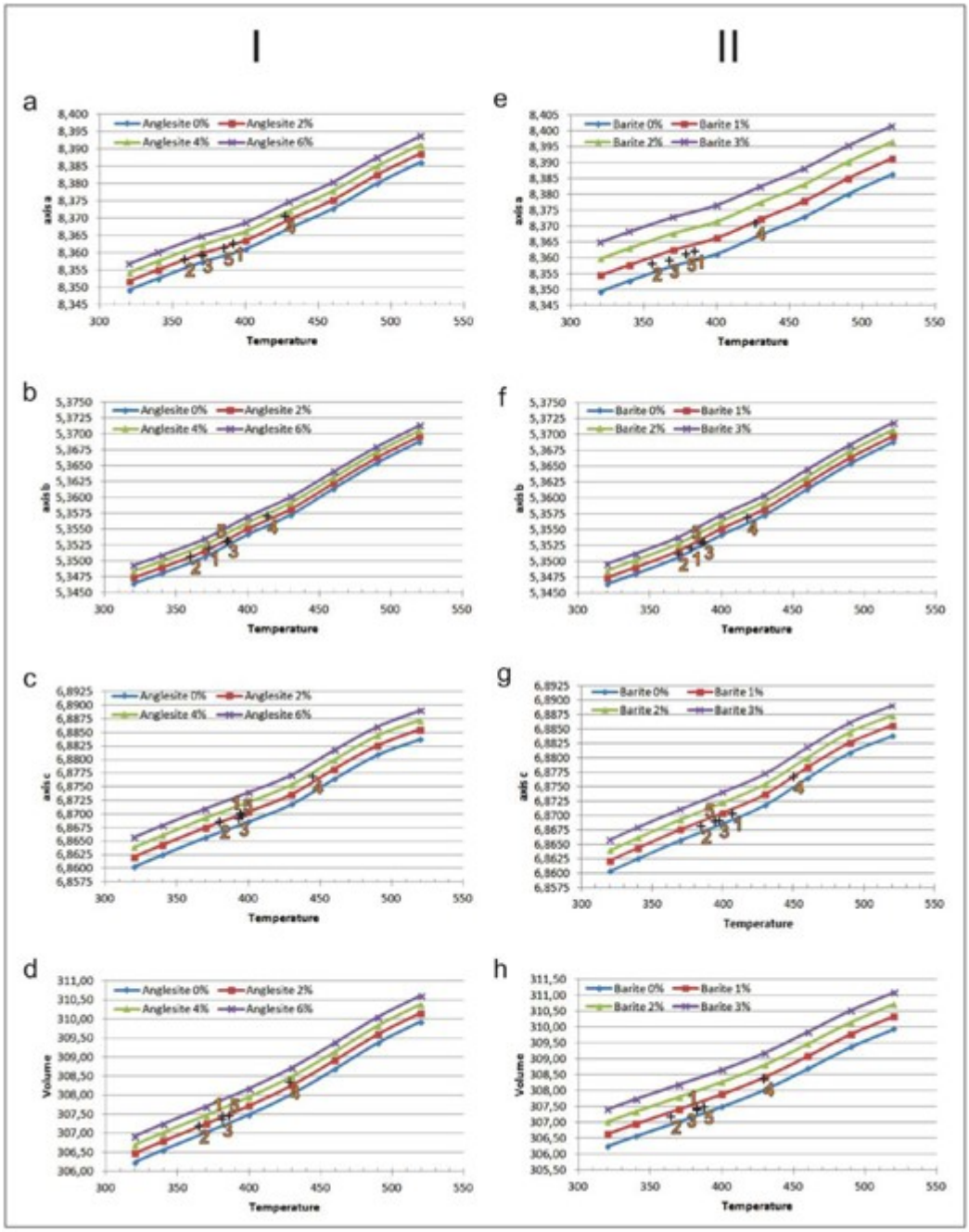

Figure 3. Variations of the temperature (in K) at the ambient pressure for the $Clt_{100}Ang_{0}$-$Clt_{94}Ang_{06}$ (column I, left) and the $Clt_{100}Brt_{0}$-$Clt_{97}Brt_{03}$ (column II, right) solid-solutions series (in mol. %), according to the recalculated unit-cell parameters (Tables S16 and S17 in the ESM): **a** & **e** axis a_0 (in Å); **b** & **f** axis b_0 (in Å); **c** & **g** axis c_0 (in Å); and **d** & **h** volume V_0 (in $Å^3$). Importantly, the proposed method can successfully be used as a geothermometer;

https://doi.org/10.1180/mgm.2023.88 Published online by Cambridge University Press

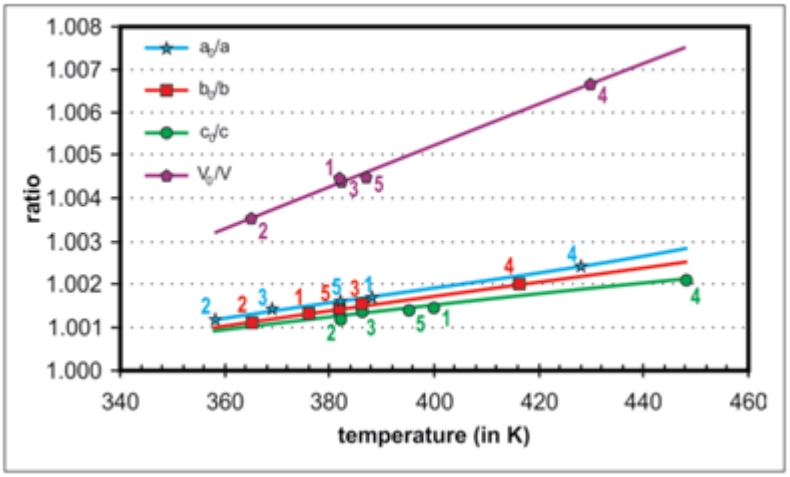

Figure 4. Temperature dependence by the relative unit-cell parameters (a_0-cyan; b_0-red; c_0-green; and V_0-purple) of the investigated 1-5 samples, at the ambient pressure conditions;

https://doi.org/10.1180/mgm.2023.88 Published online by Cambridge University Press

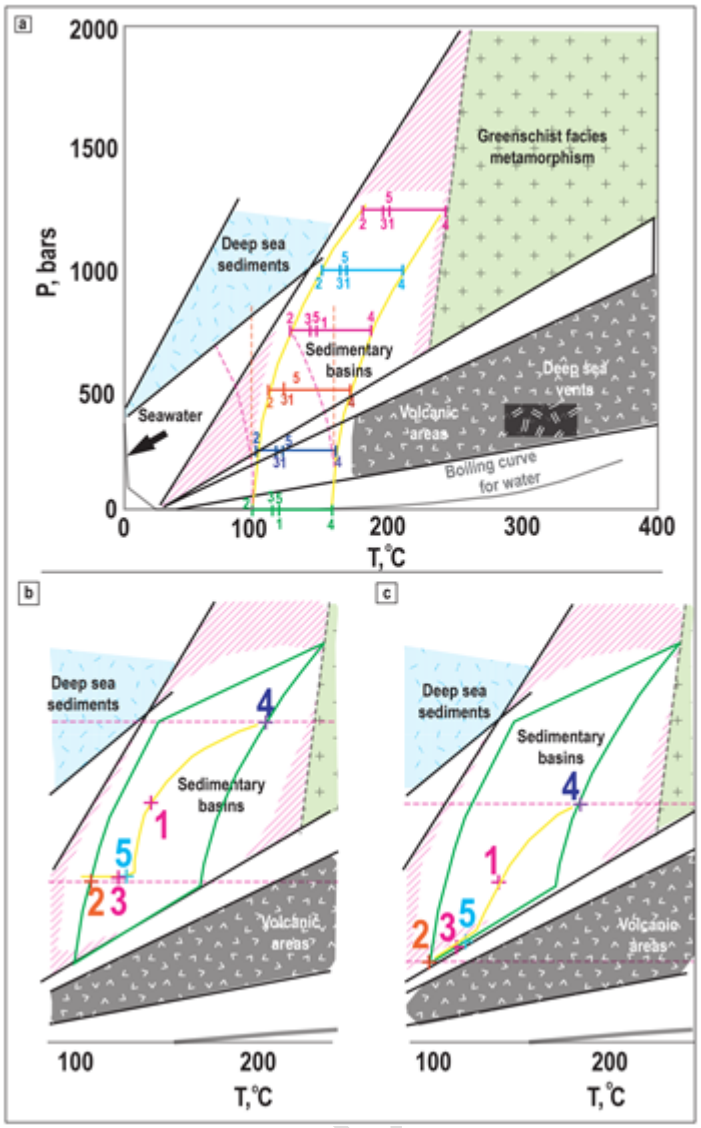

Figure 5. Pressure-temperature conditions: (a) Characterized average temperature ranges of ~368-430K (~95-157 °C) stand for all 1 to 5 investigated samples (green tick marks), having the same ambient pressure (Table 8). The sketch presents 1. temperature remains constant by the pressure increase (orange interrupted lines); 2. Temperature increases by the pressure increase (yellow full lines with approximate slope); and 3. Temperature increases by the pressure decrease (pink dotted lines with approximate slope). The presumed temperature ranges at 250, 500, 750, 1000, and 1250 bars, are represented with blue, red, purple, cyan, and magenta colors, respectively. The presumed range within sedimentary basins (green full lines) of the investigated 1-5 samples formation (yellow full lines) ranges between (b) 500 and 1000 bars (orange interrupted lines); and (c) 250 and 750 bars (orange interrupted lines). Inset was taken and modified from Hanor 2000 and refers to the shallow crustal and marine environments.

https://doi.org/10.1180/mgm.2023.88 Published online by Cambridge University Press

Table 1 The resulting WDS analyses of the 1-5 studied samples (in wt. %). Atoms per formula units (hereinafter apfu; in at. %) are calculated at the 4 oxygen anions basis.

oxides	Sample 1	Sample 2	Sample 3	Sample 4	Sample 5
SrO	55.21	54.72	54.93	54.93	54.33
CaO	0.07	0.16	0.15	0.24	0.22
BaO	0.45	0.62	0.42	0.56	0.58
PbO	1.04	0.94	0.87	1.01	0.94
SO_3	43.23	43.57	43.62	43.28	43.93
Σ	100.00	100.00	99.99	100.02	100.00
apfu	**Sample 1**	**Sample 2**	**Sample 3**	**Sample 4**	**Sample 5**
Sr	0.984	0.970	0.973	0.978	0.959
Ca	0.002	0.005	0.005	0.008	0.007
Ba	0.005	0.007	0.005	0.007	0.007
Pb	0.009	0.008	0.007	0.008	0.008
ΣM	1.000	0.990	0.990	1.001	0.981
S	1.000	1.003	1.003	1.000	1.006
ΣM+S	2.000	1.993	1.993	2.001	1.987
S/ΣM	1.000	1.013	1.013	0.999	1.025
Σ(Pb+Ba)/Σ(Ca+X)	7.000	1.000	0.800	1.875	0.577

https://doi.org/10.1180/mgm.2023.88 Published online by Cambridge University Press

Table 2 Calculated theoretical ionic radiuses (in Å) of the M cations, and calculated occupancies of the twelve-coordination site (in at. %) at the basis of the determined apfu's (Table 1).

	Sample 1	Sample 2	Sample 3	Sample 4	Sample 5	variations
r^{2+}	1.41696	1.39680	1.40112	1.40832	1.38096	5<2<3<4<1
a^{2+}	0.00268	0.00670	0.00670	0.01072	0.00938	1<2=3<5<4
a^{2+}	0.00805	0.01127	0.00805	0.01127	0.01127	1=3<2=4=5
b^{2+}	0.01341	0.01192	0.01043	0.01192	0.01192	3<2=4=5<1
r_M	1.44110	1.42669	1.42630	1.44223	1.41353	5<3<2<1<4
cc.*	1.00076	0.99076	0.99049	1.00155	0.98162	5<3<2<1<4

*-occupancies were calculated by the ΣrM/1.44Å ratios

https://doi.org/10.1180/mgm.2023.88 Published online by Cambridge University Press

Table 3 Determined contents of the trace elements (in $mgkg^{-1}$).

	Sample 1	Sample 2	Sample 3	Sample 4	Sample 5
r	10.70	6.60	0.40	3.80	<0.07
u	20.30	13.70	<0.50	1.30	2.40
a	6.96	7.36	6.87	8.24	6.98
i	0.71	1.08	0.94	0.83	1.57
r	1.61	1.38	1.51	2.25	2.15
r	<0.15	<0.15	32.3	28.6	<0.15
b	<0.71	7.09	5.61	<0.71	0.72
l	47.60	38.60	38.50	45.00	14.10
b	0.046	0.071	<0.040	<0.040	0.044
f	0.69	0.34	1.33	1.29	0.42
n	0.55	0.83	0.86	1.75	0.56
e	16.6	11.2	8.29	5.53	2.43
g	156.0	88.8	95.5	89.9	86.9
r	<0.31	<0.31	1.15	<0.31	<0.31
u	1.86	1.44	1.84	1.16	2.03
d	0.76	0.16	<0.05	1.06	0.34
m	<0.50	0.65	<0.50	<0.50	0.82
	1.	0.	<	0.	<

https://doi.org/10.1180/mgm.2023.88 Published online by Cambridge University Press

h	07	86	0.50	95	0.50
i	3.00	< 0.20	< 0.20	35.3	< 0.20
y	< 0.50	0.64	< 0.50	0.58	< 0.50
n	1.00	< 0.25	< 0.25	< 0.25	< 0.25

https://doi.org/10.1180/mgm.2023.88 Published online by Cambridge University Press

Table 4 Calculated SrSO4 mole fractions from the observed d(211) inter-planar spacings (Table S1).

	Sample 1	Sample 2	Sample 3	Sample 4	Sample 5
observed d_{211} (Å)	2.9708	2.9698	2.9704	2.9737	2.9708
$SrSO_4$ (mol. %)*	99.8	100.6	100.2	97.6	99.8

*calculated from the equation by Goldish (1989): $d(211) = 3.1023 - 0.1317 \times S$, where S is the SrSO4 mole fraction

https://doi.org/10.1180/mgm.2023.88 Published online by Cambridge University Press

Table 5 Calculated unit-cell parameters of the investigated samples in the *Pnma* space group, compared to the celestine reference data standards; and also between each other

	8 9-0953	0 5-0593	Sa mple 1	Sa mple 2	Sa mple 3	Sa mple 4	Sa mple 5	vari ations
a_0 (Å)	8 .359	8 .359	8.3 622(6)*	8. 3578(9)	8. 359(1)	8. 3705(6)	8. 361(1)	2<3 <5<1<4
b_0 (Å)	5 .350	5 .352	5.3 519(4)	5. 3510(5)	5. 353(1)	5. 3568(4)	5. 3528(8)	2<1 <3~5<4
c_0 (Å)	6 .869	6 .866	6.8 702(4)	6. 8683(7)	6. 8690(8)	6. 8767(2)	6. 8696(6)	2<3 <5<1<4
V_0 (Å^3)	3 07.27	3 07.17	30 7.46(4)	30 7.17(5)	30 7.36(8)	30 8.34(4)	30 7.47(7)	2<3 <1~5<4

*-The numbers in parentheses in this and further Tables are the estimated standard deviations (hereinafter esd's) multiplied with Scor (Berar and Lelann, 1991; Table S2 in the ESM), and refer to the last significant number

https://doi.org/10.1180/mgm.2023.88 Published online by Cambridge University Press

Table 6 The summarized IR results for the investigated samples together with the literature data

Sample					Reference						
					1*, 1a*	*	*	4*	*	*	*
48	49	48	35	40							
75	75	78	68	70	491						71
		08	02	05				610-613	13-14		
14	13	12	09	10	613		10			11	14
22	22	32	32		627	20			20		
51	42	45	41	42	642		39	641-644		43	48
55	50					50					
001	000	98	95	99	974	015	90	993-998	93	91	91
105						110					
	089		085		1081						
	100	095	090				095	1086-1096		091	
	102	115	121								
		130	128	138			130	1131-1145	133	138	138
152	151	155	150	158	1147	150			150		
				189	1179						
198	194	195	192			200	195		197	201	
210	212	205	205					1190-1207			

https://doi.org/10.1180/mgm.2023.88 Published online by Cambridge University Press

			222								
242	238	248	240	245				12 40-1250	242	248	238

References: 1* Ross (1972); 1a* Ross (1974); 2* Guirguis (1987); 3* Omori (1986); 4* Gadsden (1975), 5* Moenke (1956); 6* Kloprogge et al. (2001); and 7* Lane (2007).

https://doi.org/10.1180/mgm.2023.88 Published online by Cambridge University Press

Table 7 Dominant wavelenght (in nm) and the color purity of the investigated samples. The contents of the organic matter (in wt. %) are also presented

	Sample 1	Sample 2	Sample 3	Sample 4	Sample 5
Dominant wavelenght	481.7	482.5	494.1	480.4	489.1
Purity of the color	5.37	4.64	1.36	5.45	7.16
Organic matter	< 0.05	< 0.05	< 0.05	0.14	< 0.05

https://doi.org/10.1180/mgm.2023.88 Published online by Cambridge University Press

Table 8 The estimated formation temperature (in K) of the studied samples based on their recalculated anglesite (Ang) and barite (Brt) contents (Fig. 3)

	Sample 1		Sample 2		Sample 3		Sample 4		Sample 5		variations
	ng	rt	ng	rt	ng	rt	ng	rt	ng	rt	
mol.%	.20	.65	.18	.64	.40	.41	.10	.91	.78	.52	3<5<1~2<4
a_0 (Å)	92	85	60	56	70	68	28	27	86	78	2<3<5<1<4
b_0 (Å)	73	78	61	70	86	87	14	18	87	85	2<1<3~5<4
c_0 (Å)	94	07	80	84	93	97	45	51	96	95	2<3~5<1<4
average (axes)	87	90	67	70	83	84	29	32	89	86	2<3<1~5<4
V_0 (Å^3)	82	83	65	65	82	83	29	30	87	87	2<1~3<5<4
average (all)	86	88	66	69	83	84	29	32	88	86	2<3~1=5<4
average temperature (Ang+Brt)	387		368		384		430		387		2<3~1=5<4
axes variations	$b_0<a_0<c_0$		$a_0<b_0<c_0$		$a_0<b_0<c_0$		$b_0<a_0<c_0$		$a_0<b_0<c_0$		

https://doi.org/10.1180/mgm.2023.88 Published online by Cambridge University Press

Table 9 Relative unit-cell parameters of the investigated samples, calculated from the ratio of the data outlined in Table 5 and Table S20 in the ESM (marked here with *)

	Sample 1	Sample 2	Sample 3	Sample 4	Sample 5	sample variations
a_0/a^*	1.00170	1.00117	1.00144	1.00246	1.00156	2<3<5<1<4
b_0/b^*	1.00129	1.00112	1.00150	1.00202	1.00146	2<1<3~5<4
c_0/c^*	1.00149	1.00121	1.00146	1.00214	1.00140	2<5<3~1<4
average (axes)	1.00149	1.00117	1.00147	1.00221	1.00147	2<1~3~5<4
V_0/V^*	1.00444	1.00350	1.00444	1.00667	1.00448	2<1~3~5<4
average (all)	1.00223	1.00175	1.00221	1.00332	1.00222	2<1~3~5<4
ratio of axes variations	$b_0<c_0<a_0$	$a_0<b_0<c_0$	$a_0<c_0<b_0$	$b_0<c_0<a_0$	$c_0<b_0<a_0$	

https://doi.org/10.1180/mgm.2023.88 Published online by Cambridge University Press